

# Experimental and Computational Study of Microstructural Effect on Ductile Fracture of Hot-Forming Materials

Yang Liu<sup>1</sup>, Yiguo Zhu<sup>1,\*</sup>, Caglar Oskay<sup>2</sup>, Ping Hu<sup>1</sup>, Liang Ying<sup>1</sup> and Dantong Wang<sup>1</sup>  
1. State Key Laboratory of Structural Analysis for Industrial Equipment, Faculty of Vehicle Engineering and Mechanics, International Research Center for Computational Mechanics, Dalian University of Technology, Dalian 116024, People's Republic of China  
2. Department of Civil and Environmental Engineering, Vanderbilt University, Nashville, TN 37235

**Abstract:** Thermo-mechanical experiments at different elevated temperatures are carried out for tensile and shear-dominant specimens extracted from warm forming materials of 7075 aluminum alloy and 22MnB5 boron steel, respectively. A specimen-embedded furnace jointed by temp-control system to perform the high temperature shear experiments. Driven by microscale anisotropic plastic flow, damage is embedded in each slip system and damage evolution is controlled by the preferential dislocation slip. Combined with microscale damage and dislocation density based constitutive model, an advanced crystal plasticity method is proposed to perform predictions of mechanical behavior of face-center-cubic materials at various temperatures. Reasonable agreement is obtained between experimental and numerical results for different specimens, temperature conditions and materials. This approach simultaneously captures the strain hardening rate, damage softening, non-linear post-necking and fracture strain. Microstructural effects on ductile fracture are tracked and investigated including dislocation density and crystallographic orientation. The results show that local dislocation density rise is associated with damage initiation. Different fracture morphologies and necking paths are caused by distinct initial misorientation distributions in comparison with experimental observation of 7075 aluminum alloy. Local misorientations are investigated and critical misorientation ranges are computed for promoting void growth in zigzag and straight fracture morphologies. Schmid factor is computed as not necessary variable to trigger void growth.

## Keywords

Polycrystalline Material; Crystal Plasticity; Constitutive Behavior; Dislocation Density; Microscale Damage; Thermo-mechanical Processes;

## 1. Introduction

Warm forming and hot stamping technologies are widely used for production of lightweight, low spring back and high strength structural components [1,2]. Warm forming for aluminum alloy (AA) is usually conducted in temperature range of 473K to 623K [2] and hot stamping for boron steel (BS) is performed at 873K to 1173K [3]. At these temperature ranges, these two alloys remain mostly face-centered cubic (FCC). During thermo-mechanical loading of these two alloys, an experimental-numerical approach is proved to be effective and efficient in studying the performance of damage [4,5], strain rate and temperature effects [6–12]. To the best of our knowledge, the previous investigations were performed based on phenomenological models, and the fundamental relationships between microstructure and thermo-mechanical responses have not been established.

In metallurgical deformation of polycrystalline materials, the anisotropic plastic behavior is a

---

\* Corresponding author. Tel: 86-411-84707330, Fax: 86-411-84708390  
E-mail address: zhuyg@dlut.edu.cn

primary mechanism. Because of the crystallographic anisotropy, macroscopic phenomenon such as damage evolution, strain hardening and material yield strength is orientation-dependent [13–15]. In recent years, crystal plasticity finite element (CPFE) method has progressed as an effective scheme for modeling polycrystalline anisotropy and localized plastic flow. It has been validated by microscopic detection technologies including scanning electron microscope (SEM) [14,16,17], X-ray diffraction (XRD) [18], transmission electron microscopy (TEM) [19] and electron backscatter diffraction (EBSD) [20–25]. In combination with discrete Green's function fast Fourier transform (FFT) and spectral interpolation, CPFE model can efficiently and accurately obtain the grain-orientation-dependent mechanism at the phase or grain interface [26,27].

The interaction between void growth and dislocation mechanism is first addressed by Steven et al. concluding that dislocation nucleation may be triggered on slip planes intersecting the void at points of high shear-stress concentration [28]. In general of ductile material, the damage initiation and void nucleation are associated with stress enhancement mechanism, involving plastic flow and dislocation accumulation [29]. To implement the dislocation density in modeling large plastic deformation leading to ductile fracture, multiple constitutive models are proposed coupled with crystal plasticity. An advanced dislocation density based strain hardening law was implemented in the multiscale framework such as visco-plastic self-consistent (VPSC) and elasto-plastic self-consistent (EPSC) models to predict the anisotropic mechanical response and texture evolution of polycrystalline materials [30–34]. To consider the rate dependency and thermal effect, Knezevic et al. [35] proposed a dislocation density based model considering dislocation activity as a function of temperature and strain rate. Recently, a nonlocal CPFE model combined with dislocation based model was presented and the density distribution of geometrically necessary dislocation (GND) was explicitly captured [36] compared with experimental observation in the indentation test of single-crystalline nickel.

To model the damage initiation and ductile fracture of polycrystalline materials, a micromechanics-based model, called the Gurson–Tvergaard–Needleman (GTN) model, was developed and combined with complex constitutive models, such as visco-plasticity [37], crystal plasticity [38] and strain-gradient plasticity [39]. However, there is a need to identify multiple void-associated parameters combined with accurate microscale experimental data. Another approach is the continuum damage mechanics (CDM). Continuum damage model has been widely used for predicting damage initiation, coalescence and localization phenomena [40–43]. For instance, geometric, energetic and general CDM damage models were applied in structural steels to describe the void growth, void shape change and damage energy dissipation in different stages of damage growth [44–46]. Recently, to account for microstructural features and anisotropic properties [13,17,19], the CDM model was applied in the CPFE framework. Damage evolution coupled with CPFE could provide insight into void development at the grain scale. In Ref. [14] the capability of four simple CDM models were investigated combined with crystal plasticity.

Ductile fracture depends strongly on the extreme values of microstructural characteristics. To investigate microstructural effects on ductile fracture, computational models have been developed such as sensitive analysis [47], image-based finite element analysis [48] and micromechanical modeling [49,50]. Modeling and investigations are mainly focused on the heterogeneous effect of inclusion or void morphologies [47,48,50] and disperse distributions [39]. However, these micromechanical-based analysis does not account for the mechanical anisotropy, specifically the heterogeneity in polycrystalline microstructures. Recently, the damage evolution is assisted by

classical crystal plasticity model to study the effect of non-basal slip in ductile fracture at different loading directions [51]. But the positive role of microstructural effects on high-temperature ductile fracture still lack investigation.

The primary goal of this study is to deepen the understanding of the characteristics for underlying microstructural variables including the (1) crystallographic orientation and the (2) dislocation density and their effects on the damage initiation and ductile fracture at elevated temperatures. A micro-damage model is proposed as a function of the accumulated local shear strain in the slip system. Incorporated with the damage model, a dislocation density based crystal plasticity can capture the observed plastic deformation localization, local stress concentration, dislocation pile-ups and void growth within the microstructure. The remainder of this paper is organized as follows. The material properties and experimental setups are introduced in Section 2. Coupled with directional micro-damage model, the temperature-dependent crystal plasticity framework is provided in Section 3. The numerical implementation is illustrated in Section 4. Calibration and verification of this continuum micro-damage mechanics coupled crystal plasticity finite element model (CPFE-CDM) are provided for the two alloys in Section 5. The dislocation density distributions and orientation characteristics are investigated with fracture morphologies and damage distributions for microstructural analyses in Section 6 and conclusions are provided in Section 7.

## 2. Experimental Setups

In the experimental aspect, EBSD was conducted to study the phase distribution, orientation-based microstructure, misorientation data and grain size of 7075 AA and 22MnB5 at room temperature. To investigate the ductile fracture under elevated temperature of these two alloys, thermo-mechanical tests were performed and approximate uniform temperature fields were applied in the large deformation region of the specimen. In addition, SEM was conducted to understand the morphology and features of the fracture surface.

From the in-situ EBSD measurements, the initial texture of 7075 AA with FCC lattice are obtained as shown in Fig. 1(a), which are similar to previous observations [52]. The initial microstructure in 7075 AA mainly contains equiaxed grains and some elongated grains in the rolling direction. Zn, Cu and Mg are the main alloying elements to form the small precipitates. Since the micron-scale void growth is studied in context, the precipitates within scales of ten nanometers are negligible. The mean grain size of 7075 AA is 103.4 $\mu\text{m}$  and its grain size barely changes in the thermal condition, even heating to 773K. The initial microstructure of as-received 22MnB5 consists of mainly ferrite and pearlite. Pre-heating of the specimen at 900°C for 5 minutes before tests ensures that the grain microstructures are fully transformed into austenite FCC crystal structure with random orientation distribution, as shown in Fig. 1(b). These austenite grains are mostly equiaxed and their mean grain size is approximately 90 $\mu\text{m}$ .

In the thermo-mechanical test, uniform temperature field is applied in the large deformation region of the specimen. For thermal tensile and shear tests, two kinds of thermal heating equipment are employed as shown in Fig. 2 and 3. and three duplicates are conducted for each test to ensure the validity of the experiments. The traditional vertical tensile testing is not suitable for the thermal experiments due to gravity effect. Thus, horizontal thermal heating equipment is adopted. In thermal tensile test of 7075 AA shown in Fig. 2, a thermocouple is attached close to the middle section of the specimen, and the temperature is maintained for 3 minutes by the temperature controlled system. An extensometer is installed on the specimen to measure the thermal strain. The mechanical curves

of 7075 AA are shown in Fig. 4(a). In order to be completely austenized by the heating process, the 22MnB5 BS shear specimen is placed in the heating furnace in Fig. 3. The white inside the furnace is asbestos for preventing heat transfer and preserving heat. Since the specimen is contained in the furnace, extensometer is hard to attach onto the shear specimen. Thus, in the shear tests of 22MnB5 BS, the stress-versus-strain curves are replaced by force-versus-displacement ones in Fig. 4(b).

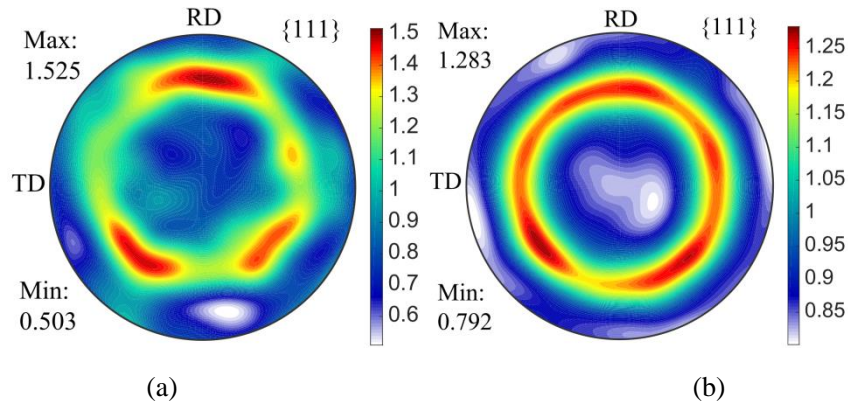


Fig. 1 Initial orientation distributions in pole figures: (a) 7075AA; (b) 22MnB5 steel

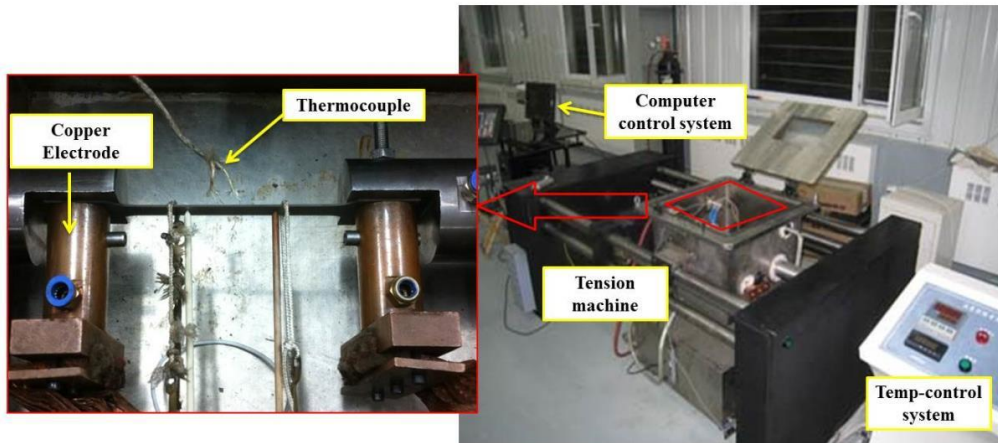


Fig. 2 The thermal tensile experiment with the thermocouple attached to the specimen and the temperature-control system (tensile test for 7075 AA and 22MnB5 BS)

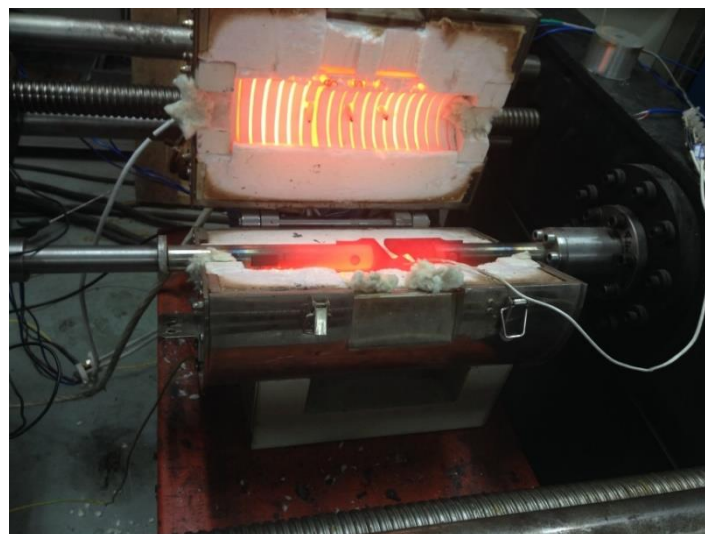


Fig. 3 The thermal shear equipment with the heating furnace. Heat preserving asbestos (white) and horizontal mechanical stretcher are incorporated (shear test for 22MnB5 BS)

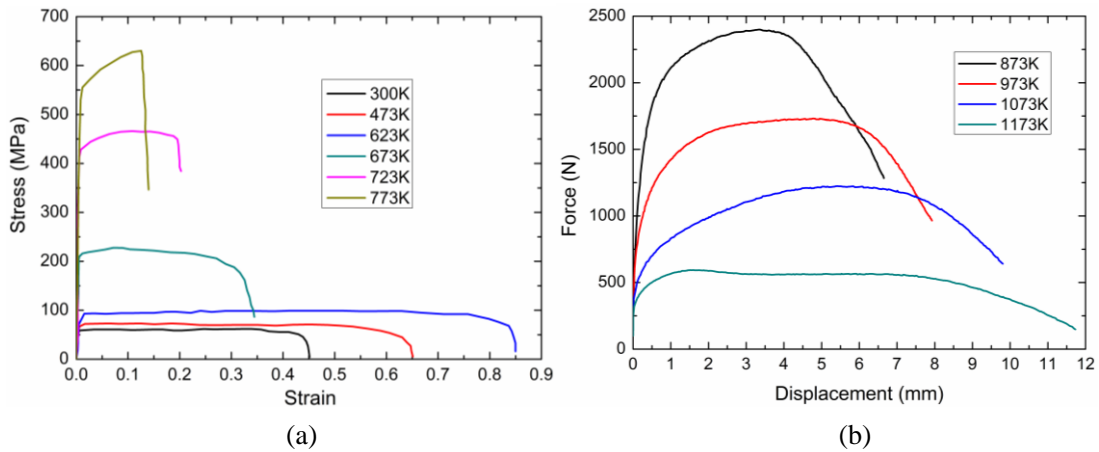
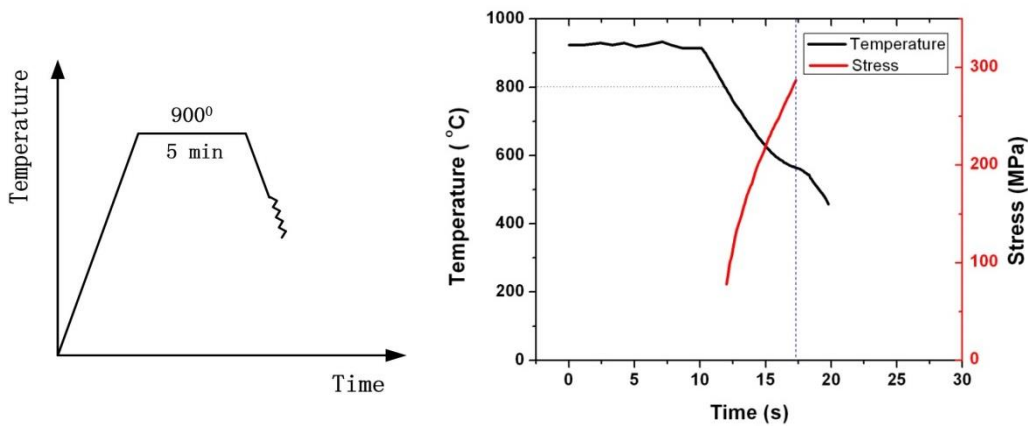


Fig. 4 The mechanical curves in thermo-mechanical tests. (a) engineering stress-strain curves of 7075 AA; (b) force- versus-displacement curves of 22MnB5.

In the realistic hot stamping process, phase transformation may happen due to excessive cooling rate during stamping. As a schematic temperature variation shown in Fig. 5 (a), the temperature of 22MnB5 sheet is maintained at approximately  $900^{\circ}\text{C}$  for 5 minutes in furnace for austenite preparation. Then the sheet is directly transferred into stamping step. After stamping, the temperature of the sheet is lowered down to room temperature and phase transformation from austenite to martensite occurs during this step to obtain high strength and hardness of the material. It should be noted that temperature drops during stamping because the sheet exchanges heat with air, which may induce phase transformation at this step and cause potential damage due to high hardness of martensite. As an example, at an excessive cooling rate of  $43.9^{\circ}\text{C/s}$  in Fig. 5(b), the tangent of temperature curves experiences a small fluctuation at 17.5s, where the phase transition point is about  $570^{\circ}\text{C}$  and the damage occurs.

To resolve this problem, suitable temperature cooling rate is maintained by heating the die and punch to stabilize the austenite phase. At a suitable temperature cooling rate of  $33.6^{\circ}\text{C/s}$ , thermal tensile tests of 22MnB5 BS are conducted to recreate the non-transformation situation in the stamping process. The specimens are maintained at  $800^{\circ}\text{C}$  and  $700^{\circ}\text{C}$  for 5 minutes and then the stretcher begins to operate while the temperature drops at the same time. The mechanical curves are shown in Fig. 5 (c) and the approximate linear hardening in the plastic region is induced by the increase of elastic moduli and strength when temperature drops.



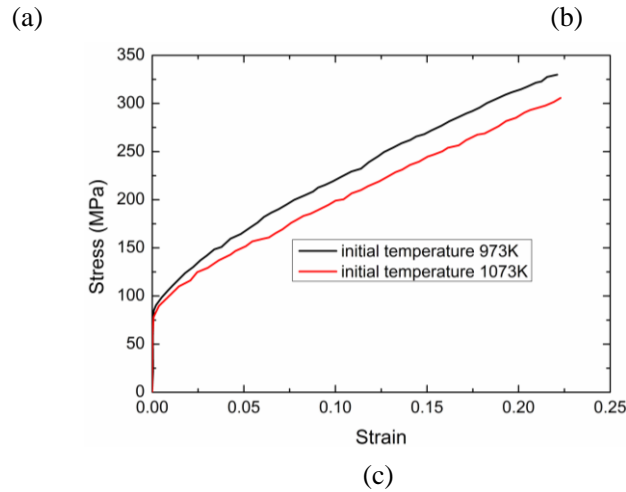


Fig. 5 The temperature variation process of 22MnB5 in hot stamping. (a) Schematic temperature evolution in hot stamping; (b) The nonlinear stress descending due to phase transformation during temperature variation (initial temperature of 900°C); (c) Mechanical curves of two initial temperature conditions in tensile test with cooling rate of 33.6°C/s.

To understand the microstructural evolution in the material under thermal tensile or shear tests, the SEM is used to analyze the fracture surface in each specimen. Partial fracture surface of the 7075 AA tensile specimens using SEM is shown in Fig. 6 (a). The rough fractured surface is constructed by small dispersoids (dimples) with serrated shape, which results in void growth and coalescence. These dimples with the serrated features show that the dimples are enlarged by the localized dislocation flow. Dislocation piles up at the grain boundary to form a micron-scale void, and the void forms at the intersection of the grain boundary. This implies that inter-granular damage occurs near grain boundaries in 7075 AA with intense dislocation mobility. In the zoomed-in Fig. 6 (b), the void nucleates and the cavity is embedded within the serrated features near the grain boundary.

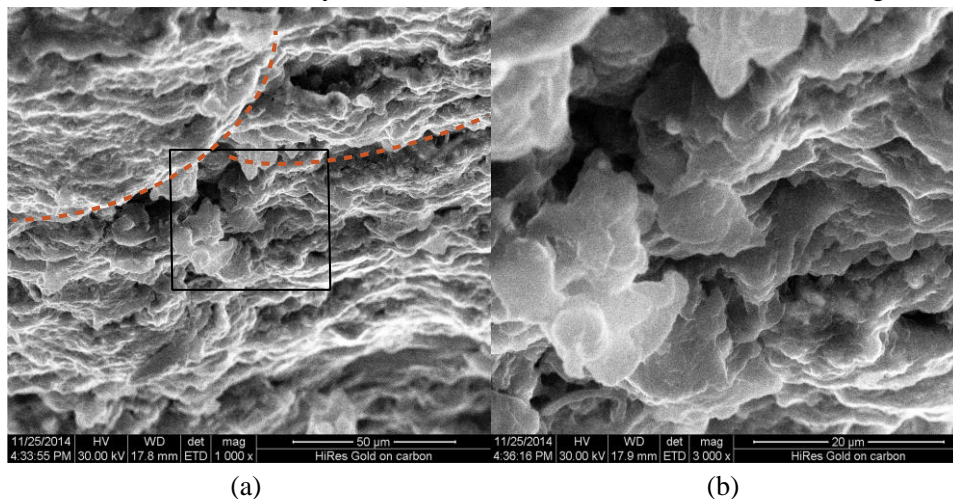


Fig. 6 The fracture surfaces of the 7075 AA tensile specimen at 473K in SEM. (b) is the amplified version of the black square region in (a). Yellow dash line is the grain boundary.

The fracture surfaces of 22MnB5 BS after thermal shear test are examined by SEM and shown in Fig. 7. Multiple large dimples are formed and surrounded by small dimples, which indicates severe ductile fracture inside the material. Aided by localized plastic flow, the clustered small

dimples grow and coalesce into big ones. Subsequently, damage initiation occurs inside these dimples. In the zoomed-in image of one large dimple, clear micro-damage paths are generated inside. The dimple with approximate length of 40  $\mu\text{m}$  and depth of 5 $\mu\text{m}$  reveals severe local plastic deformation near fracture region.

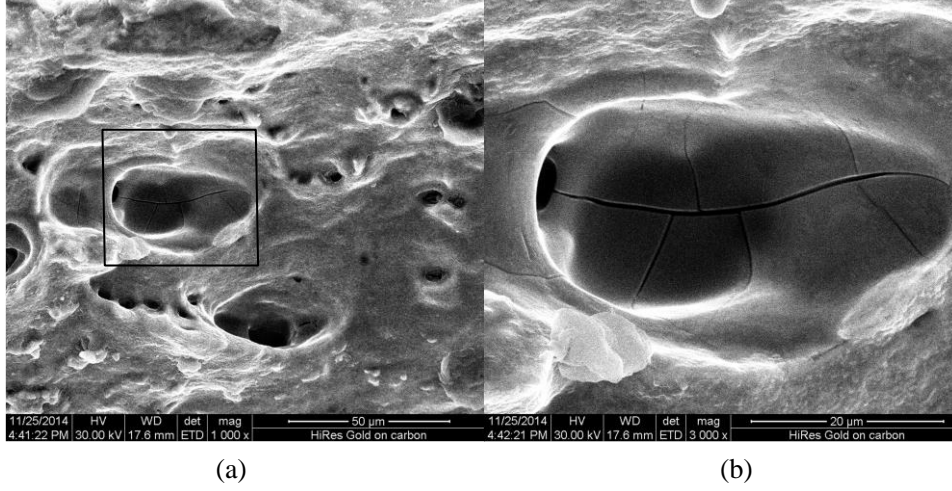


Fig. 7 The fracture surfaces of the 22MnB5 BS shear specimen at 1183K in SEM. (b) is the amplified version of the black square region in (a).

### 3. Thermo-mechanical crystal plasticity model coupled with directional damage

In this section, the advanced crystal plasticity model is developed accounting for the two-way coupling between temperature field and mechanical field. The dislocation density based hardening rule is applied to consider the dislocation barrier inside single crystal. A micro-damage model is proposed to model the directional void growth induced by preferential dislocation slip. The thermal and strain rate effects are coupled in the damage process. Heat generation induced by plastic dissipation is incorporated in the thermo-mechanical model.

#### 3.1 Kinematics

Considering the presence of high temperatures and associated thermal strains, the total deformation gradient  $\mathbf{F}$  is decomposed into three terms, elastic, plastic and thermally-induced deformation gradients [53],

$$\mathbf{F} = \mathbf{F}^e \mathbf{F}^p \mathbf{F}^\theta \quad (1)$$

where,  $\mathbf{F}^e$  represents the reversible lattice distortion and rigid rotation.  $\mathbf{F}^p$  accounts for the irreversible incompressible plastic deformation gradient related to pure slip,  $\det(\mathbf{F}^p) = 1$ .  $\mathbf{F}^\theta$  is the isothermal deformation gradient related to the thermal expansion at each material point.

The material derivative of plastic deformation gradient leads to its evolution equation,

$$\dot{\mathbf{F}}^p = \mathbf{L}^p \mathbf{F}^p \quad (2)$$

where,  $\mathbf{L}^p$  is the plastic velocity gradient, which is formulated according to the physical representation of the dislocation sliding by

$$\mathbf{L}^p = \sum_{\alpha} \dot{\gamma}^{\alpha} \bar{\mathbf{P}}^{\alpha}, \quad \bar{\mathbf{P}}^{\alpha} = \mathbf{s}^{\alpha} \otimes \mathbf{m}^{\alpha}. \quad (3)$$

The Schmid tensor  $\bar{\mathbf{P}}^{\alpha}$  is constructed using the slip direction  $\mathbf{s}^{\alpha}$  and the slip plane normal  $\mathbf{m}^{\alpha}$  of the  $\alpha$ th slip system. In this kinematic formulation, the plastic shear strain rate  $\dot{\gamma}^{\alpha}$  represents the geometrical deformation of each crystalline slip system, which is correlated with the evolution of dislocation density mobility in the following section.

The velocity gradient  $\mathbf{L}$ , associated with total deformation gradient, could be decomposed to describe the crystallographic reorientation and stretch rate,

$$\mathbf{L} = \dot{\mathbf{F}} \cdot \mathbf{F}^{-1} = \mathbf{D} + \mathbf{\Omega} \quad (4)$$

Here,  $\mathbf{D}$  is the symmetric stretch rate tensor and  $\mathbf{\Omega}$  is the antisymmetric spin tensor. The latter term contains the elastic lattice spin  $\mathbf{\Omega}^e$  and the plastic spin  $\mathbf{\Omega}^p$ , and  $\mathbf{\Omega}^p$  is a skew-symmetric component of plastic velocity gradient  $\mathbf{L}^p$ .

$$\mathbf{\Omega} = \mathbf{\Omega}^e + \mathbf{\Omega}^p, \quad \mathbf{\Omega}^p = \frac{1}{2}(\mathbf{L}^p - \mathbf{L}^{pT}) = \sum_{\alpha=1}^n \mathbf{\Omega}^\alpha \dot{\gamma}^\alpha, \quad \mathbf{\Omega}^\alpha = \frac{1}{2}(\mathbf{s}_0^\alpha \otimes \mathbf{m}_0^\alpha - \mathbf{m}_0^\alpha \otimes \mathbf{s}_0^\alpha) \quad (5)$$

Here  $\mathbf{\Omega}^\alpha$  is the plastic spin tensor defined on the  $\alpha$ th slip system. In this rate-dependent crystalline constitutive framework, the Jaumann rate  $\dot{\hat{\boldsymbol{\sigma}}}$  of Cauchy stress  $\boldsymbol{\sigma}$  is used to describe frame objective stress evolution,

$$\dot{\hat{\boldsymbol{\sigma}}} = \boldsymbol{\varphi} : \mathbf{D} - \boldsymbol{\sigma}(\mathbf{I} : \mathbf{D}) \quad (6)$$

where  $\boldsymbol{\varphi}$  is a fourth-rank elastic moduli tensor and  $\mathbf{I}$  is the identity matrix of rank two. Then, the equation is further derived as

$$\dot{\hat{\boldsymbol{\sigma}}} = \boldsymbol{\varphi} : \mathbf{D} - \dot{\boldsymbol{\sigma}}^0 - \text{tr}(\mathbf{D})\boldsymbol{\sigma}. \quad (7)$$

Here,  $\dot{\boldsymbol{\sigma}}^0$  is a reference stress rate associated with shear strain rate on each slip system of the crystal and  $\text{tr}(\mathbf{D})$  denotes the trace of matrix  $\mathbf{D}$ .

### 3.2 Kinetics and dislocation density based hardening rule

Since temperature-dependent plasticity is considered in the microscale crystallographic mechanical behavior, a physics-based exponential evolution equation is employed to describe the local shear slip rate  $\dot{\gamma}^\alpha$  on the  $\alpha$ th slip system using thermal activation mechanism [53],

$$\dot{\gamma}^\alpha = \frac{\rho_m v_{id} b^2}{2} \exp\left(\frac{-\Delta F}{k\theta}\right) \exp\left(\frac{(\tau^\alpha - s^\alpha)\Delta V}{k\theta}\right) \quad (8)$$

Here,  $\Delta F$  is the Helmholtz free energy, or the effective activation energy barrier for dislocation glide.  $\rho_m$  is the mobile dislocation density determined by the volume fraction of precipitates in the material,  $v_{id}$  the dislocation vibration frequency,  $b$  the magnitude of the Burgers vector,  $k$  the Boltzmann constant and  $\theta$  the absolute temperature. The pinning distance  $l$ , also called the jump width, is of the same order of magnitude as the thermal activation length  $d$ , leading to the right term of this equation.  $\Delta V$  is the activation volume, proportional to  $lb^2$  and the jump width  $l$  is given by  $1/(\rho_{GND} + \rho_{SSD})^2$  [54,55]. Since the sum of the GND and statistically stored dislocation density (SSD) are dependent on the dislocation length, a length scale dependent slip rule could be employed to study the effects of grain size dependence. It should be noted that the slip rate  $\dot{\gamma}^\alpha$  is activated when the resolved shear stress (RSS)  $\tau^\alpha$  is higher than its critical value, the critical resolved shear stress (CRSS)  $s^\alpha$ , otherwise  $\dot{\gamma}^\alpha = 0$ .

The microscale hardening on the  $\alpha$ th slip system is affected by the current temperature, the shear strain rate  $\dot{\gamma}^\alpha$  and dislocation density evolution (Knezevic et al., 2013a), which forms a dislocation density based hardening model for the FCC crystal. In what follows, the superscript  $\alpha$  used to indicate the specific slip system is omitted for simplicity. For each slip system, the CRSS  $s(\dot{\gamma}, \theta)$  related with shear strain rate and temperature is decomposed into four terms according to different contributing mechanisms: including friction stress  $s_{0,f}(\theta)$ , Hall-Petch-associated term  $s_{0,HP}(\theta)$ , the forest dislocation term  $s_{for}(\dot{\gamma}, \theta)$  and the debris dislocation term  $s_{deb}(\dot{\gamma}, \theta)$  [56].

$$s(\dot{\gamma}, \theta) = s_{0,f}(\theta) + s_{0,HP}(\theta) + s_{for}(\dot{\gamma}, \theta) + s_{deb}(\dot{\gamma}, \theta) \quad (9)$$

Friction stress  $s_{0,f}(\theta)$  depends on the Peierls-Nabarro stress, softened by increasing temperature.

$$s_{0,f}(\theta) = \mu(\theta) \exp\left(-\frac{2\pi w}{b}\right) \quad (10)$$

where,  $w$  is the dislocation width, defined as  $a/(1-\nu)$ . The inter-planar spacing  $a$  is the characteristic lattice constant and  $\nu$  is the Poisson's ratio.  $\mu(\theta)$  is the shear modulus related with current temperature state. The grain size resistance term  $s_{0,HP}(\theta)$  is correlated with initial average grain size  $d_g$  via Hall-Petch-like relationship and decreases with increasing temperature through  $\mu(\theta)$  [56],

$$s_{0,HP}(\theta) = \mu(\theta) HP \sqrt{\frac{b}{d_g}} \quad (11)$$

where  $HP$  is the Hall-Petch parameter. This form of temperature dependence has been previously shown in experimental tests for FCC polycrystalline metals [57].

Temperature softening of shear modulus  $\mu(\theta)$  is introduced with increasing temperature, modeled as [58],

$$\mu(\theta) = \mu_0 - \frac{H}{\exp(\theta_0/\theta) - 1} \quad (12)$$

in which,  $\mu_0$  is an initial shear modulus at temperature  $\theta_0$ .  $H$  and  $\theta_0$  are material constants. The feasibility and applicability of this function to elastic stiffness constants are demonstrated in conjunction with the mechanical threshold stress model [59,60].

Slip resistance terms  $s_{for}$  and  $s_{deb}$  are related to dislocation density increase due to boundary trapping [32]. The dislocation mobility inside crystal results in two types of boundaries: geometrically necessary boundary (GNB) and statistically stored boundary (SSB); the dislocation density increases near these boundaries. GNB occurs as plastic strain accumulates by unevenly distributed slip and subsequently the cell blocks form. Whereas SSB forms inside cell blocks because of the interactions between various slip systems. The latent hardening effect is implicitly coupled in these substructures through thermally activated processes including dislocation climb and cross slip, which leads to a lower energy barrier between the cells, also called a cell wall. The two kinds of sub-boundaries and the dislocation induced cell structures inside the single FCC grain are schematically illustrated in Fig. 8.

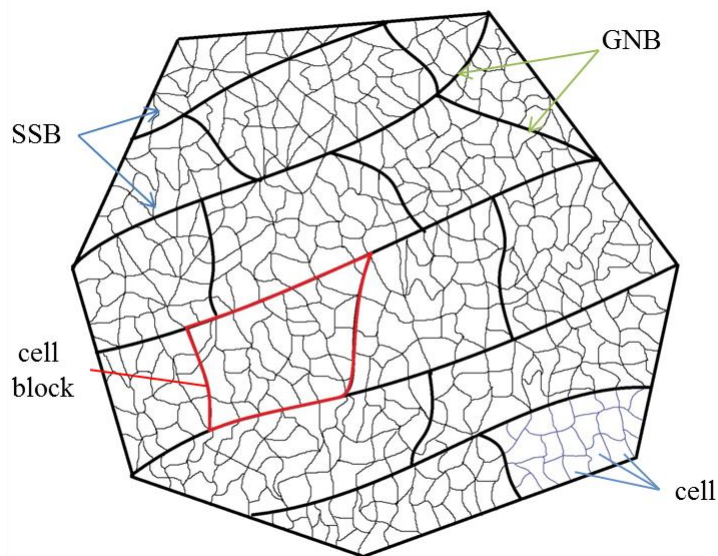


Fig. 8 The schematic microscopic grain substructures: cell block formed inside grain and connected by GNB; cells generated in the cell block and separated by SSB.

The densities of the spatially randomly distributed forest dislocations, also called SSD [61,62] are denoted as  $\rho_{\text{for}}$  and the debris dislocations, known as GND are denoted as  $\rho_{\text{deb}}$ . GNDs usually address the size dependence and the accumulation of GNDs have an important influence on the deformation gradient in CPFE simulations [54,63,64]. Here, GND and SSD are combined to describe the dislocation density accumulation associated with different kinds of dislocation boundaries in Fig. 8. Here, the corresponding strength components associated with dislocation densities are expressed as,

$$s_{\text{for}} = \mu(\theta)b\chi\sqrt{\rho_{\text{for}}} \quad (13)$$

$$s_{\text{deb}} = k_{\text{deb}}\mu(\theta)b\sqrt{\rho_{\text{deb}}}\log\left(\frac{1}{b\sqrt{\rho_{\text{deb}}}}\right) \quad (14)$$

in which,  $\chi$  is a dislocation interaction constant chosen as 0.9 to not introduce extra slip mode for  $s(\dot{\gamma}, \theta)$  [65];  $k_{\text{deb}}$  is a mathematical material-independent constant, set as 0.086, to ensure that the strain rate function covers the Taylor law at low dislocation density [35,56,66]. The forest dislocation density evolution is controlled by the storage rate  $\frac{\partial\rho_{\text{gen}}}{\partial\gamma}$  and the recovery rate  $\frac{\partial\rho_{\text{rec,for}}}{\partial\gamma}$ .

$$\frac{\partial\rho_{\text{for}}}{\partial\gamma} = \frac{\partial\rho_{\text{gen}}}{\partial\gamma} - \frac{\partial\rho_{\text{rec,for}}}{\partial\gamma} = k_1\sqrt{\rho_{\text{for}}} - k_2(\dot{\gamma}, \theta)\rho_{\text{for}} \quad (15)$$

where,  $k_1$  is an adjustable coefficient for the generating of statistically stored dislocation (SSD) due to forest dislocation trapping of mobile dislocation.  $k_2$  is the rate-sensitive coefficient for dynamic recovery in thermal activation mechanism, which is given by,

$$k_2(\dot{\gamma}, \theta) = k_1\frac{b\chi}{g}\left[1 - \frac{k\theta}{\bar{D}b^3}\ln\left(\frac{\dot{\gamma}}{\dot{\gamma}_0}\right)\right] \quad (16)$$

where,  $\dot{\gamma}_0$ ,  $g$ ,  $\bar{D}$  are, respectively, the reference strain rate, the stress-independent activation energy and the drag stress.  $\chi$  is the same dislocation interaction constant in Eq. (13). Here  $\dot{\gamma}_0$  is set as  $10^7$  for each slip modes and applicable for different strain rate ranges [65]. The stress-independent activation energy  $g$  and the drag stress  $\bar{D}$  are obtained from the optimization process of the fitting tests in Section 4.3.

Debris dislocation evolution is defined as [65],

$$\Delta\rho_{\text{deb}} = q(\theta)b\sqrt{\rho_{\text{deb}}}\frac{\partial\rho_{\text{rec,for}}}{\partial\gamma}\Delta\gamma \quad (17)$$

where  $q(\theta)$  is rate coefficient defining the fraction of dislocations that do not annihilate but stored as debris, which is exponentially changing with the temperature (Knezevic et al., 2013a).

$$q(\theta) = E\exp\left(-\frac{\theta-\theta_{\text{ref}}}{F}\right) \quad (18)$$

here,  $E$  and  $F$  are constants associated with  $\{111\}\langle 110\rangle$  slip system.

The general and advanced strain hardening stages in single crystal deformation behaviors of FCC crystals are presented in Fig. 9(a) and 9(b), respectively. In this study, the dislocation density based hardening model coupled with thermally activated recovery and sub-grain strengthening is used to consider not only strain hardening, but also slip climb and cross-slip. This extends the strain hardening up to stage IV in Fig. 9(b). The stage IV hardening is correlated with various microstructural features, such as grain refinement, texture evolution, orientation mismatch, and spacing between GNDs [65,67]. It should be noted that the stage IV activation process could be enhanced by increase in temperature and decrease in strain rate, and becomes the predominant factor in large strain deformation. Thus, the temperature-dependent dislocation activated model is

employed to model the thermo-mechanical behavior in stage IV hardening.

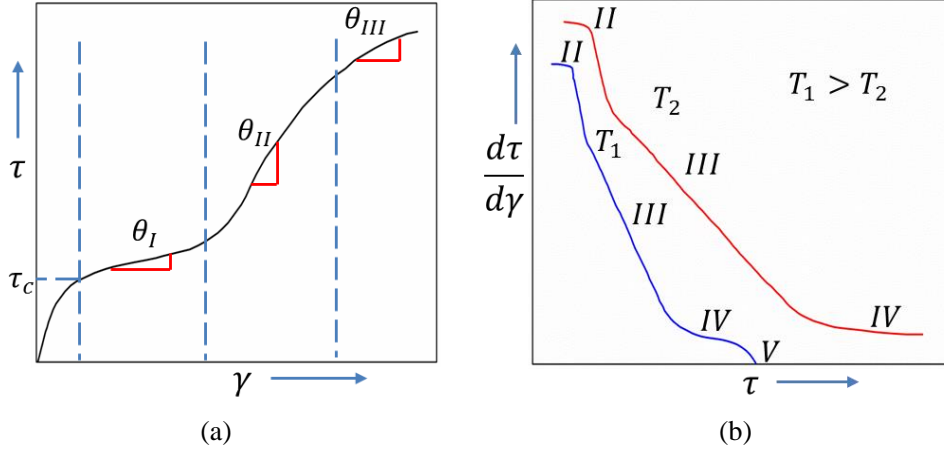


Fig. 9 The schematic hardening process in crystalline slip systems (a) shear stress versus shear strain in hardening process for FCC slip systems; (b) instantaneous ratio (shear stress divided by shear strain) versus shear stress in two temperature conditions.

### 3.3 Temperature-consistent microscale damage

Microscopically, Hagihara et al. [16] confirmed that dislocation slip has a major influence on void development and two voids that are close together would not coalesce preferentially if dislocation slip is not favorably activated through them. To consider these microstructural features, a CDM model is proposed and defined at the scale of material microstructure. The micron-scale damage was embedded in each dislocation slip and the physics-based microstructural variable of accumulated slip of the corresponding slip system, was determined to govern the direction and evolution of damage variable in the single crystal. The damage evolution at elevated temperature is characterized by the Zener-Hollomon factor.

In this study, void growth along the dislocation slip direction is the main concern and the void state is defined by the damage variable  $D$ . In crystal plasticity, the flow stress in one slip system is influenced by the current damage via the resolved shear stress (RSS) measure [68]

$$\tau_D^\alpha = \frac{\tau^\alpha}{1-D^\alpha} = \frac{T:\bar{P}^\alpha}{1-D^\alpha}, \quad (19)$$

where  $D^\alpha$  is the damage variable on the  $\alpha$ th slip system and  $T$  is the 2<sup>nd</sup> Piola-Kirchhoff (P-K) stress.  $\tau_D^\alpha$  is the effective RSS acting on the damaged material at the  $\alpha$ th slip system. The void state is strongly coupled with stress field at each increment. When  $D^\alpha = 0$ , the micron void does not exist in the slip system. As soon as  $D^\alpha > 0$ , damage initiation happens and voids begin to nucleate and grow along the preferential direction of the  $\alpha$ th dislocation slip. The fracture happens when the spatial damage distribution spreads across the transverse direction of the sample. Since the damage state is defined on each slip system, the maximum damage induced by preferential dislocation slip dominates the void state inside one single crystal. Thus, the damage in one material point is computed as  $\max(D^\alpha)$ . The damage in this model is considered as micro-damage, since its evolution is controlled by dislocation slip within the grain length scale of micron for both 7075 AA and 22MnB5 BS.

The void growth and coalescence are strongly influenced by plastic anisotropy in FCC crystals, which causes the damage anisotropy. In previous CDM models, damage anisotropy is considered by two-rank or four-rank tensors [42,69]. In this study, preferential dislocation slip is considered as

the main effect on the direction of void growth and coalescence. The preferential directions of void expansion in each single crystal are associated with preferential slips inside crystals. For example, when void densities of two adjacent grains increases at their grain boundary due to intense dislocation pile-ups, the voids begin to coalesce and generate high stress concentration near the grain boundary. The influence of crystallographic anisotropy on void evolution patterns is discussed in Section 5.2.

The temperature and strain rate effects are considered in the evolution function of damage. The strength softening caused by void growth is coupled with the current temperature state  $\theta$  and strain rate  $\dot{\epsilon}$  by introducing the Zener-Hollomon factor  $Z$  [70].

$$Z = \dot{\epsilon} \exp\left(\frac{\Delta F}{k\theta}\right) \quad (20)$$

The thermally activated damage in  $\alpha$ th slip system is then expressed as,

$$D^\alpha = \begin{cases} 0 & \gamma^\alpha \leq \gamma_{ini}^\alpha(Z) \\ D_{max} \left( \frac{\gamma^\alpha - \gamma_{ini}^\alpha}{\gamma_{max}^\alpha - \gamma_{ini}^\alpha} \right)^M & \gamma_{ini}^\alpha(Z) < \gamma^\alpha < \gamma_{max}^\alpha(Z), \\ D_{max} & \gamma^\alpha \geq \gamma_{max}^\alpha(Z) \end{cases} \quad (21)$$

where  $\gamma_{ini}^\alpha$  and  $\gamma_{max}^\alpha$  are accumulated slip when the void nucleates and reaches its maximum density value  $D_{max}$ , respectively. Since FCC crystal has only one kind of slip system  $\{111\}[110]$ , the maximum density value is assumed the same in different slip directions. The threshold values of maximum shear strain,  $\gamma_{ini}^\alpha$  and  $\gamma_{max}^\alpha$ , are functions of  $Z$ . In this model, the void growth differs on each slip system due to distinct dislocation flow and the void enlargement at one material point depends on the damage of all slip systems. In this way, the crystallographic orientation has its important influence on the plasticity-aided ductile fracture at elevated temperature.

### 3.4 Temperature increase in plastic dissipation

In previous sections, the effect of temperature and strain rate is already considered in the elasto-plastic behavior and material softening. The current temperature state has the influence on damage evolution through Eq. (20) and on crystallographic shear strain through Eq. (8). In this section, the reserve effect of heat generation by plastic dissipation is incorporated in the large plastic deformation mechanism to ensure the two-way coupling. Here, the partial energy is stored in the plastic deformation since the lattice distortion preserves the energy in pure slip deformation. The total dissipation rate  $\psi$  per unit volume in the reference configuration compared with the current stage is given by

$$\psi = -\rho_0 \dot{\epsilon} + \mathbf{P} : \dot{\mathbf{F}} + \rho_0 \theta \dot{\eta} - \Phi \nabla \theta, \quad (22)$$

where  $\rho_0$  is the referential mass density,  $\dot{\epsilon}$  the internal energy density rate,  $\mathbf{P}$  the 1<sup>st</sup> P-K stress,  $\dot{\eta}$  the entropy rate,  $\Phi$  the entropy flux and  $\nabla \theta$  the gradient of temperature. Combined with Eq. (1), Eq. (22) is expressed as,

$$\mathbf{P} : \dot{\mathbf{F}} = \mathbf{P} \mathbf{F}^{\theta T} \mathbf{F}^{p T} : \dot{\mathbf{F}}^e + \sum_\alpha \tau^\alpha \dot{\gamma}^\alpha + \mathbf{F}^{p T} \mathbf{F}^{e T} \mathbf{P} : \dot{\mathbf{F}}^\theta. \quad (23)$$

The relationship between resolved shear stress (RSS)  $\tau^\alpha$  and the 1<sup>st</sup> P-K stress  $\mathbf{P}$  is,

$$\tau^\alpha = \mathbf{F}^{e T} \mathbf{P} \mathbf{F}^{\theta T} \mathbf{F}^{p T} : \bar{\mathbf{P}}^\alpha. \quad (24)$$

Dissipation  $\psi_p$  and  $\psi_{other}$ , due to plastic deformation and other inelastic deformation, are defined as,

$$\psi_p = \sum_{\alpha} \tau^{\alpha} \dot{\gamma}^{\alpha}, \quad \psi_{\text{other}} = -\rho_0 \dot{\epsilon} + \rho_0 \theta \dot{\eta} - \Phi \nabla \theta + \mathbf{P} \mathbf{F}^{\theta T} \mathbf{F}^{p T} : \dot{\mathbf{F}}^e + \mathbf{F}^{p T} \mathbf{F}^{e T} \mathbf{P} : \dot{\mathbf{F}}^{\theta}, \quad (25)$$

respectively.

As for metal deformation process, the heat produced by elastic deformation is negligible and the predominant temperature rise is induced by plastic deformation. Here the plastic deformation power is used to calculate the temperature rise while ignoring the remainder of other inelastic deformation power [71].

$$\rho_0 c \dot{\theta} = k \psi_p + \text{Div}(h \nabla \cdot \theta) - \Phi \nabla \theta \quad (26)$$

where,  $c$  is the specific heat and  $h$  is the ratio between inelastic deformation power and the plastic deformation power, which is in the range of 0.85 to 1.0 [72]. Here,  $h$  is chosen as 0.9.  $\nabla \cdot \theta$  is the divergence of the temperature field. The entropy flux  $\Phi$  is associated with the heat variation, which is defined as,

$$\Phi = \int \frac{\Delta Q}{\theta}, \quad \Delta Q = c M \Delta t \quad (27)$$

where,  $dQ$  is the heat variation,  $M$  the mass and  $\Delta t$  the time variation. The dissipation due to thermal plastic deformation is calculated by Eq. (23) to (25) and the temperature state are updated through Eq. (26) and (27) at the end of each time increment.

#### 4. Computational implementation

Implicit finite element method and an advanced explicit time integration algorithm are introduced in this section. Time step size control is applied in the algorithm.

##### 4.1 Finite Element Method

The finite element method is applied to calculate a full-field mechanical response. Accounting for both strain compatibility and stress equilibrium through the discretized virtual work principle, we obtain,

$$\left( \int_V \mathbf{B}^T \mathbf{J} \mathbf{B} dV \right) \Delta \mathbf{U} = \mathbf{R} - \int_V \mathbf{B}^T \boldsymbol{\sigma} dV \quad (28)$$

$$\mathbf{J} = \frac{\partial \delta \boldsymbol{\sigma}}{\partial \delta \boldsymbol{\epsilon}} \quad (29)$$

where,  $\mathbf{B}$  is strain-displacement relation matrix from compatibility equations,  $\mathbf{J}$  is the material-associated Jacobian matrix in terms of the tangent moduli in stress-versus-strain curves and  $\mathbf{R}$  is the applied external force vector. The Jacobian matrix could be derived directly by analytically solving  $d\boldsymbol{\sigma} = \frac{\partial \delta \boldsymbol{\sigma}}{\partial \delta \boldsymbol{\epsilon}} d\boldsymbol{\epsilon}$  coupled with a forward time integration method, provided by [73,74] and the integration procedure is introduced in the following section.

In the CPFE framework, the constitutive model is leveled from micro to macro scale. At the macro-scale, the polycrystalline response is predicted by the homogenization model, finite element method. At the micro-scale, the thermal activation mechanism is introduced in the shear strain activation function and the micro-damage evolution is considered within the preferential dislocation slip. Besides, the strengthening of grain substructure is modeled by dislocation density based hardening. The extended CPFE-CDM model has been implemented within the commercial finite element platform called ABAQUS, where hot forming and other engineering applications are usually simulated for nonlinear analysis of static and dynamic conditions. The constitutive formula of crystal plasticity and micro-damage evolution are incorporated into the platform using a user

defined subroutine named UMAT. Combined with the instantaneous updated temperature state, the microscale responses are calculated within UMAT at each time increment to analyze thermo-mechanical behavior of AA and BS.

#### 4.2 Time integration method with temperature and damage components

In order to calculate the Jacobian Matrix, a forward Euler time integration method is applied to calculate the increment of shear strain on  $\alpha$ th slip system coupled with a linear interpolation,

$$\Delta\gamma^{(\alpha)} = \Delta t[(1 - \hat{\chi})\dot{\gamma}^{(\alpha)}(t) + \hat{\chi}\dot{\gamma}^{(\alpha)}(t + \Delta t)] \quad (30)$$

Here, the interpolation control parameter  $\hat{\chi}$  is defined as 0.35 to constrain the increasing portion of the shear strain in a reasonable range, which consequently achieves better convergence rate in the integration. The dislocation-density-based hardening law leads to the indirect relationship between CRSS and shear strain rate. Consider the thermal condition and micro-damage mechanics, the shear strain increment on each slip system is decomposed by the following formula including the effect from temperature and micro-damage variables,

$$\Delta\gamma^{(\alpha)} = \Delta t\left(\dot{\gamma}^{(\alpha)}(t) + \hat{\chi}\frac{\partial\dot{\gamma}^{(\alpha)}}{\partial\tau^\alpha}\Delta\tau^\alpha + \hat{\chi}\frac{\partial\dot{\gamma}^{(\alpha)}}{\partial\theta}\Delta\theta + \hat{\chi}\frac{\partial\dot{\gamma}^{(\alpha)}}{\partial D^\alpha}\Delta D^\alpha\right) \quad (31)$$

Here, the local strain concentration, or localized plastic flow could be induced by both severe void growth and preferential dislocation slips in the polycrystalline material. The total strain increment of the  $n$ -th time step is then calculated as,

$$(\Delta\gamma)_n = \sum_{\alpha} |(\Delta\gamma^{(\alpha)})_n| \quad (32)$$

For an increment, the variations of forest and debris dislocation density are calculated by their initial values at the beginning of this increment. To simply describe the incremental form of dislocation density based hardening, the number of slip system  $\alpha$  is omitted in the following equations.

$$(\Delta\rho_{\text{for}})_n = \left(\frac{\partial\rho_{\text{for}}}{\partial\gamma}\right)_n (\Delta\gamma)_n = k_1\sqrt{(\rho_{\text{for}})_n} - k_2(\dot{\gamma}, \theta)(\rho_{\text{for}})_n \quad (33)$$

$$(\Delta\rho_{\text{deb}})_n = qb k_2(\dot{\gamma}, \theta)\sqrt{(\rho_{\text{deb}})_n}(\rho_{\text{for}})_n(\Delta\gamma)_n \quad (34)$$

$$(\rho_{\text{for}})_{n+1} = (\Delta\rho_{\text{for}})_n + (\rho_{\text{for}})_n \quad (35)$$

$$(\rho_{\text{deb}})_{n+1} = (\Delta\rho_{\text{deb}})_n + (\rho_{\text{deb}})_n \quad (36)$$

Then at the end of this increment, CRSS is updated for the next time step using following equation,

$$s(\dot{\gamma}, \theta)_{n+1} = \mu(\theta) \exp\left(-\frac{2\pi w}{b}\right) + \mu(\theta) \text{HP} \sqrt{\frac{b}{d_g}} + \mu(\theta) b \chi \sqrt{(\rho_{\text{for}})_{n+1}} + k_{\text{deb}} \mu(\theta) b \sqrt{(\rho_{\text{deb}})_{n+1}} \ln\left(\frac{1}{b\sqrt{(\rho_{\text{deb}})_{n+1}}}\right) \quad (37)$$

The modified forward Euler integration method coupled with the one-step update of dislocation density is able to separate the evolution of shear strain rate and CRSS, and the analytical solution of Jacobian can be obtained. This integration method requires a reasonable time step to satisfy the current stability criterion. In this study the time step is revised in each increment to obtain a better convergence rate. Because of high nonlinearity in exponential strain rate function, the relatively small change of CRSS in one time step could lead to high variation of shear strain rate increment. Thus, the expected strain rate increment is controlled in each step according to ratio parameter  $R = \Delta\gamma_{\text{max}}^\alpha / \Delta\gamma_s$  between the maximum shear strain increment  $\Delta\gamma_{\text{max}}^\alpha$  in one element and a reference

value  $\Delta\gamma_s = 1.0 \times 10^{-4}$ . If the  $\Delta\gamma_{max}^\alpha$  is higher than 1.25, then a lower increment  $\Delta t/R$  is used to recalculate the variable at the current time step.

## 5. Verification and Calibration of CPFEE-CDM model in RVE investigation

Representative volume element (RVE) simulations are employed to determine the thermal- and damage-associated material parameters. The temperature of 7075 AA ranges from 300K to 773K. In order to obtain fully transformed austenite grains of FCC crystal, the temperature of 22MnB5 BS ranges from 873K to 1173K. The parameters related to the thermal activated mechanism are determined by the jump tests for both materials, introduced by Hu et al. 2016 and others are fitted by the RVE calculation compared to the thermo-mechanical curves.

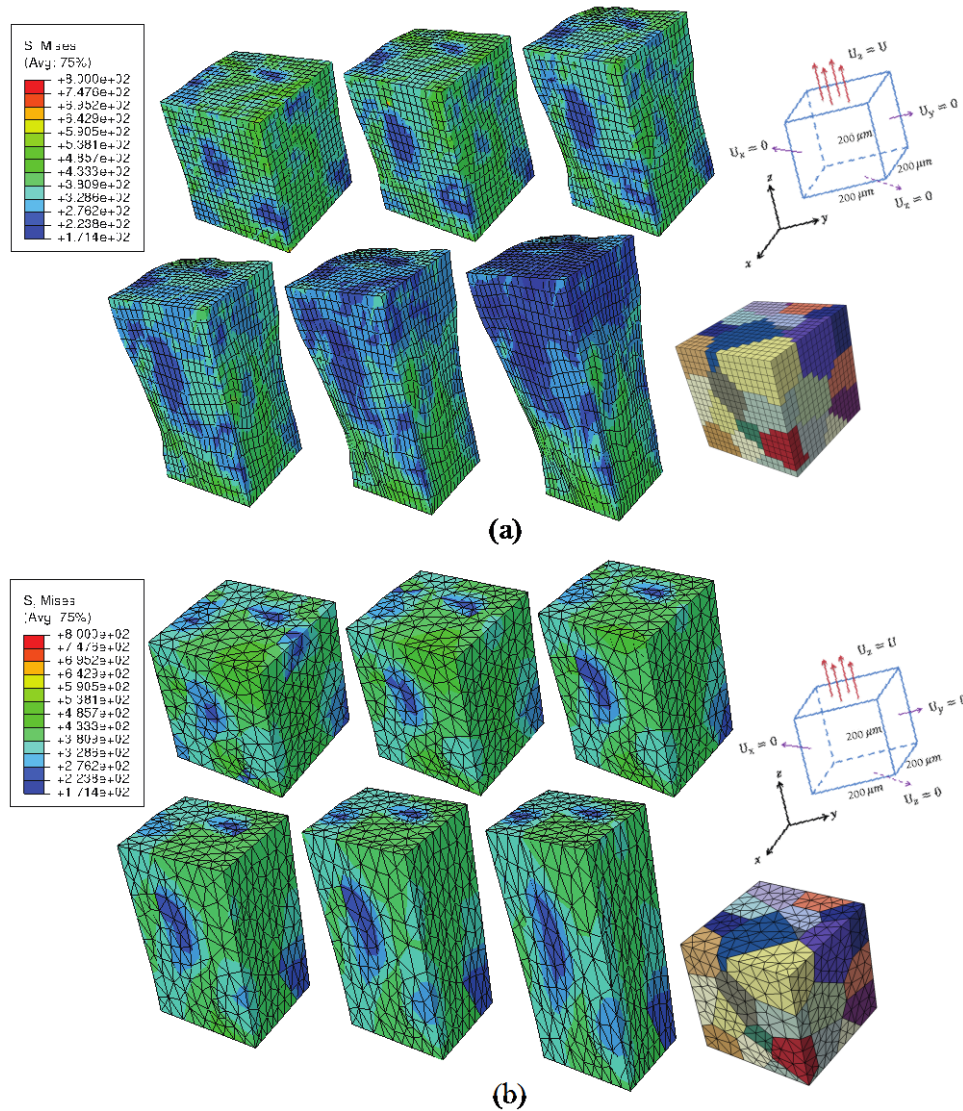


Fig. 10 The real time-dependent stress distribution patterns in two mesh types with strain steps of 0.167, 0.334, 0.501, 0.668, 0.835 and 1.000 for 6061 AA at 473K. (a) Hexahedral element; (b) Tetrahedral element. The hexahedral mesh of the polycrystal is built based on the mapping scheme compared with tetrahedral mesh [75] to obtain similar sub-grain morphology.

### 5.1 Mesh type evaluation in RVE simulation

The sub-grain structure of the RVE polycrystalline aggregate is built by using Voronoi tessellation

and realistic polycrystalline morphologies are obtained. The tetrahedral elements are usually used to mesh the grains of the polycrystalline and they are suitable for partitioning unsmooth grain boundaries. However, the tetrahedral elements are typically too stiff for describing the finite deformation of large strain and may degrade accuracy in calculating the evolution of grain morphology after severe plastic deformation [76]. As an example, hexahedral elements are employed to calculate the RVE responses and compared with the response of tetrahedral elements under uniaxial loading in Fig. 10. To create a similar sub-grain morphology in hexahedral mesh, mapping method is used to obtain the polycrystalline aggregates with serrated grain boundary in Fig. 10(a) [75]. It should be noted that the local orientation distribution are the same for these two mesh types and no damage evolution is considered in this simulation. The material property of 6061 AA from Hu et al. 2016 is applied in the simulation.

The stress contours of two meshes are shown in Fig. 10 for a number of strain steps. For 50 sub-grains in the RVE, 4913 and 5659 elements are used in hexahedral (C3D8) and tetrahedral (C3D4) mesh, respectively. Full integration is used in all simulations. In relatively small strain steps, local stress responses are similar whereas significant differences occur after total strain step is larger than 0.501. In addition, surface morphology changes severely within the hexahedral mesh in large strain step, whereas tetrahedral mesh results in almost rectangular deformed shape. Stress distributions show that hexahedral elements have the advantage of high precision to calculate local mechanical response, since eight integration points are employed in hexahedral element.

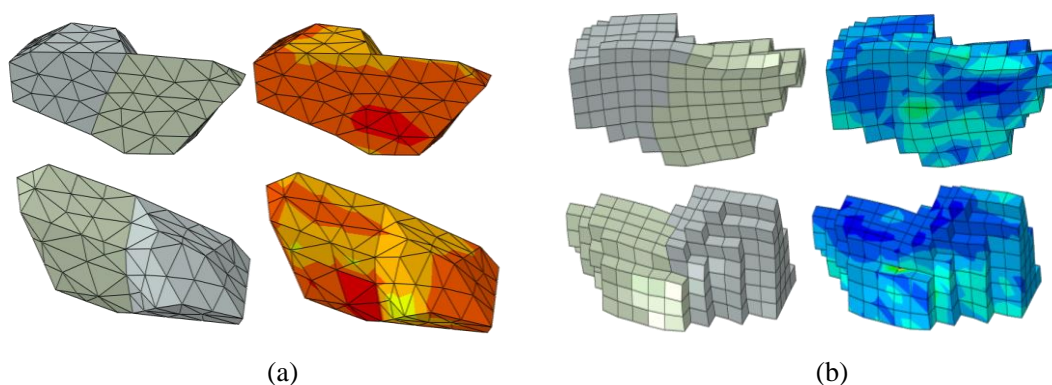


Fig. 11 The stress distribution of two local surface grains for both tetrahedral and hexahedral mesh at the same spot with strain step of 0.668.

Two local surface grains from the same spots of hexahedral and tetrahedral mesh are studied in Fig. 11 at the strain step of 0.668. Due to more degrees of freedom, the local morphology deformed more in the hexahedral element. The local stress concentrations near the grain boundary are observed in both mesh types and the grain interaction are captured among adjacent grains. The grain boundary is better captured using tetrahedral mesh whereas hexahedral mesh usually causes serrated boundary features. Thus, the tetrahedral element is generally chosen in grain boundary investigation and interfacial modelling in CPFEE analyses [77,78]. However, in another sense, the hexahedral mesh is able to reveal surface roughening in microscale. For example, Rossiter et al., (2013) used the hexahedral element to analyze the surface roughness correlated with the strain accommodation capability of various grain orientations. Recently, the stabilized tetrahedral elements are developed to overcome the volumetric locking problem in tetrahedral element and to calculate reasonable displacement response [80,81], which can reasonably capture both grain interactions and localized

plastic deformation.

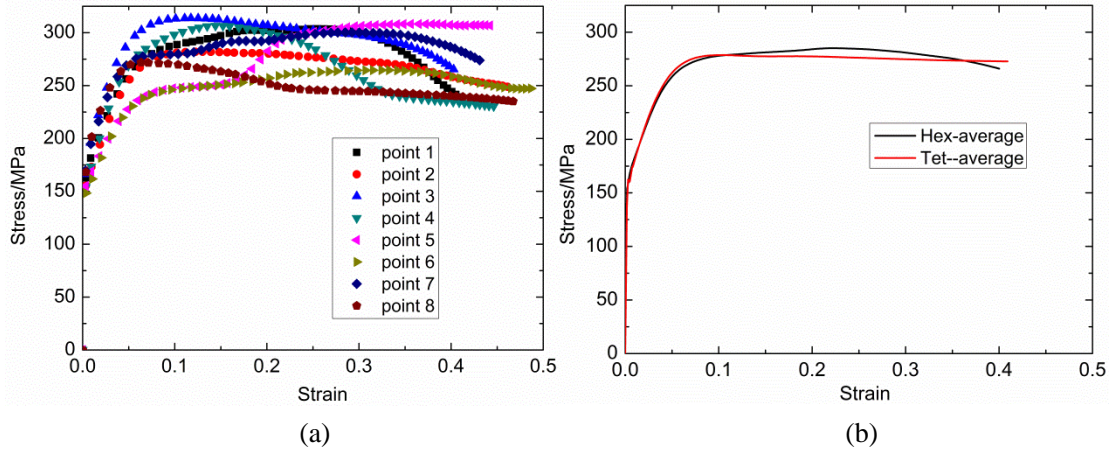


Fig. 12 The RVE simulation of mesh type comparison: (a) stress versus strain curves of eight integration points in one hexahedral element; (b) comparison of macroscopic mechanical response between the hexahedral and tetrahedral element in averaged stress versus strain curves.

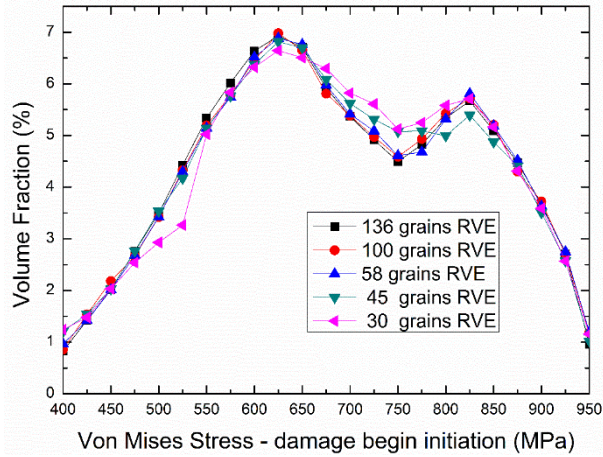


Fig. 13 The statistical Von Mises stress distribution using different RVE sizes for tetrahedral element. Each stress bin covers the range of 50 MPa and the volume fraction is stored in each bin.

The variation of the local stress-strain behavior within a single element of the hexahedral mesh is illustrated in Fig. 12(a) for eight integration points. In view of the significant variations within the element, the local mechanical response fields are described more accurately using the hexahedral mesh. Fig. 12(b) shows the overall stress-versus-strain behavior of one local grain for these two meshes with acceptable minor variation of 5.36% (Mesh variation of overall stress-versus-strain curve for the whole RVE is 2.54% and the variation is defined as  $\frac{\int_0^{\epsilon} |\sigma_{\text{hex}} - \sigma_{\text{tet}}| d\epsilon}{\int_0^{\epsilon} |\sigma_{\text{hex}}| d\epsilon}$ ). Tetrahedral

discretization has more computational efficiency compared to the hexahedral mesh. The total calculating time ratio between hexahedra and tetrahedral element is 1.672 for 50 grains aggregates under uniaxial loading. Thus, tetrahedral mesh is employed in the calibration process in Section 5.3 to obtain overall stress-versus-strain curve that matches the experimental data. The hexahedral mesh is used in the simulation process to ensure accurate local plastic deformation field compared with realistic morphology in shear and tensile test in Section 6. Above all, since directional micro-damage is incorporated in this study, the full integration hexahedral element could capture the void

growth pattern and void localization spots more accurately in the polycrystalline material with large plastic deformation.

The local stress responses are calculated for five microscale RVEs with 30-136 grains in Fig. 13 and the tetrahedral element is used. The local stress level is divided into 22 bins with width of 50 MPa and the volume fraction is collected for each stress bin. In Fig. 13, the local stress distribution deviates in RVEs with low grain number of 30 to 45 and it becomes stable after 58 grains RVE. This indicates that the convergence of local stress distribution is reached for the microstructure with 58 or more grains. Compared to the result of 136 grains RVE, the relative error is defined for both mesh types as  $\sum_{i=1}^{N_{bin}} |VF_{num}(i) - VF_{136}(i)|$ . The direct error comparisons are shown in Tab. 1. It explicitly shows that convergence of the local stress distribution is obtained when the number of grains reaches 58 inside the RVE. Therefore, the 58 grains RVE is set as the preferable RVE size for the calibration process in Section 5.3 to acquire both accuracy and efficiency.

Table 1 Error of hexahedral and tetrahedral elements in local stress distribution

Grain number in RVE	30	45	58	100
Error for Hex (%)	8.46	4.32	1.84	1.93
Error for Tet (%)	7.24	4.54	2.26	2.30

## 5.2 Anisotropic damage evolution study

In this section, the time-dependent evolutions of anisotropic damage are calculated for the 58 grains RVE when the displacement conditions changes in different directions. The local damage evolution direction varies according to the preferential dislocation flow of grains with different crystallographic orientations. The material property of 6061 AA [53] with damage evolution is used in the simulation. The RVE microstructure, material property and initial orientation distribution remain the same for (a), (b) and (c) in Fig. 14.

For 6061 AA at 473K, the loading configurations applied to the RVE and the corresponding damage contours are shown in Fig. 14. 5209 elements of C3D8 are used in the simulation with no reduced integration. The results show that void growth and coalescence among grains are quite sensitive to load orientation although the same uniaxial displacement control is applied in these cases. In this model, void growth or damage evolution is mainly aided by local dislocation slip and the direction of void expansion is strongly influenced by the preferential dislocation slip direction. When the boundary condition changes from Fig. 14 (a) to (b) or (c), the Schmid tensor  $\bar{\mathbf{P}}^\alpha$  in Eq. (3) changes in each slip system, which leads to different preferential slip and accumulated shear strain. Thus, distinct void growth and coalescence path occurs in each individual grain. This microscopic phenomenon is reflected in the macroscopic test of 7075 AA in section 6.2 and the void pattern changes with orientation and misorientation distributions.

## 5.3 Parameter calibration in the CPFE-CDM model

This section focuses on the calibration of temperature and damage coupled material parameters of the extended dislocation density based crystal plasticity model for AA and BS using the experimental data generated in this study along with those available in the literature. Specifically, thermal tensile experiments of 300K, 673K and 773K have been employed to calibrate the crystal plasticity model parameters for 7075 AA, whereas thermal shear experiments of 873K and 1073K

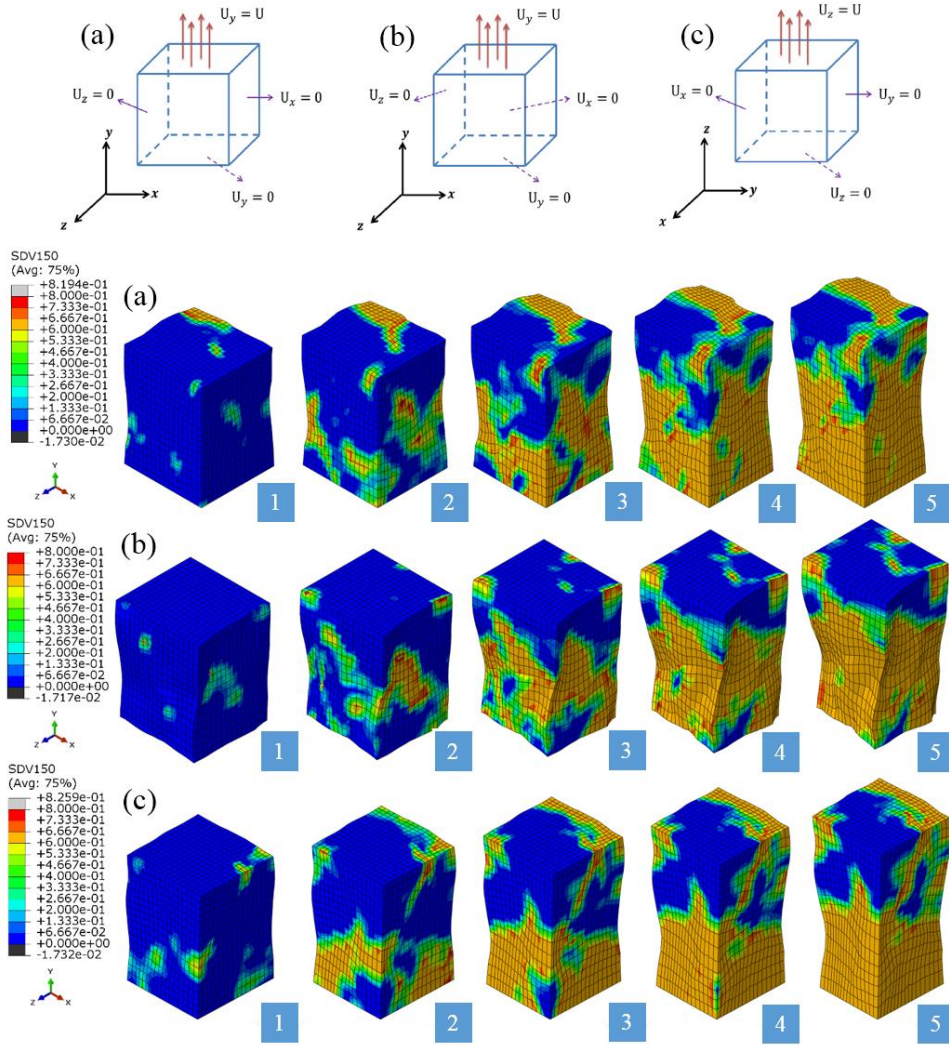


Fig. 14 Damage evolution of 6061 AA under three boundary conditions at 473K. Load steps from 1 to 5 means total strain from 0.1 to 0.5 with increment of 0.1. The length of the RVE is 1 and the boundary conditions are given as:

- (a)  $U_x = 0$  at  $x = l$ ,  $U_y = 0$  at  $y = 0$ ,  $U_z = 0$  at  $z = l$ ,  $U_y = U$  at  $y = l$ ;
- (b)  $U_x = 0$  at  $x = 0$ ,  $U_y = 0$  at  $y = 0$ ,  $U_z = 0$  at  $z = 0$ ,  $U_y = U$  at  $y = l$ ;
- (c)  $U_x = 0$  at  $x = l$ ,  $U_y = 0$  at  $y = l$ ,  $U_z = 0$  at  $z = 0$ ,  $U_z = U$  at  $z = l$ .

have been used to calibrate 22MnB5. The thermal activation related parameters,  $\Delta F^\alpha$ ,  $\Delta V^\alpha$  in Eq. (8) are calibrated by a set of jump experiments for aluminum alloy and boron steel, which is rigorously described in our previous work [53]. The elastic modulus  $\mu_0$  at initial temperature  $\theta_0$ , temperature-sensitivity parameter  $H$  in Eq. (12) and Hall-Petch associated parameter  $HP$  in Eq. (11) are defined in the literature [22,52,82]. The dislocation density based physical parameters  $g$ ,  $\hat{D}$  and  $k_1$  in Eq. (16);  $E$  and  $F$  in Eq. (18) and damage associated parameters are calibrated by fitting the simulation results of polycrystalline aggregates with the experimental curves using least-square fit optimization method. The parameters of void growth are obtained as  $\gamma_{ini}^\alpha = 0.0345Z^{0.0510}$ ;  $\gamma_{max}^\alpha = 0.0376Z^{0.0493}$  and  $\gamma_{ini}^\alpha = 0.0156Z^{0.0353}$ ;  $\gamma_{max}^\alpha = 0.0175Z^{0.0342}$  for 7075 aluminum alloy and 22MnB5 steel, respectively.  $D_{max}$  is calibrated as 0.78 for both materials to improve numerical convergence upon material softening during the necking region. All the

crystal plasticity related parameters are shown in Tab. 2 and 3.

58 grains RVE with 4913 elements are used in the calibration study. The mechanical curves are analyzed in three stages for the purpose of parameter calibration, elastic stage, strain hardening stage, and necking stage. Each stage is assumed to be separately controlled by several corresponding parameters, shown in Fig. 15. Parameters in each region are identified by the multi-objective optimization using Gaussian process [83,84]. The ISIGHT optimization software combined with ABAQUS platform is applied to perform the optimizations. The computational efficiency is increased by calibrating parameters independently in each region to fit the experimental data, whereas parameters in other regions are fixed. When the optimization in one stage is finished, the obtained parameters are transferred into optimization process in the other stage. Then, the intersections of the parameter ranges from each stage are used to fit the overall curves with a single set of deterministic parameters. When using the three-region optimization method shown in Fig. 15, a discontinuous tangent near the descending part is detected, which is not satisfactory for simulation of mechanical behavior. We combine the strain hardening (B) and necking regions (C) to improve the tangent convergence between hardening and necking behavior and continuous mechanical behavior is obtained, shown in Fig. 16 and 17. In spite of nearly triple calibration time, by using two-region method in optimization, the average error between CPFE and experiment decreases from 5.89% to 3.61% in 7075 AA and from 8.92% to 6.65% in 22MnB5 BS (error in each curve is defined as  $\frac{\int_0^\varepsilon |\sigma_{CPFE} - \sigma_{\text{experiment}}| d\varepsilon}{\int_0^\varepsilon |\sigma_{\text{experiment}}| d\varepsilon}$  OR  $\frac{\int_0^u |F_{CPFE} - F_{\text{experiment}}| du}{\int_0^u |F_{\text{experiment}}| du}$ ). The errors are shown for both methods at different temperatures in Tab. 4. In this way, the calibration of the overall curves is improved and a better global minimizer is obtained.

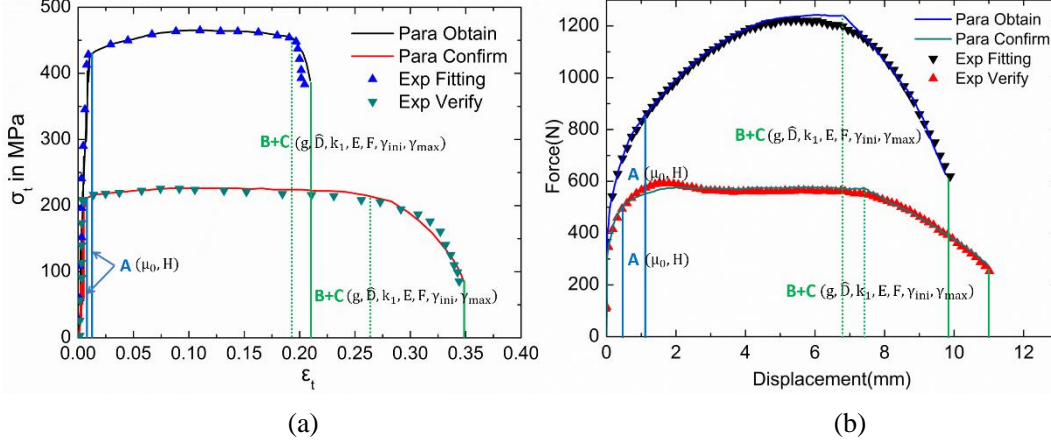


Fig. 15 Schematic two-region calibration method for 7075 AA (a) and 22MnB5 BS (b) to alleviate discontinuity between strain hardening and necking parts. The regions show different deformation processes in RVE calculation (A: elastic stage; B: strain hardening stage; C: necking stage).  $\sigma_t$  and  $\varepsilon_t$  are the engineering stress and strain for tensile experiment, respectively.

Table 2 Calibrated parameters of the crystal plasticity model for 7075 AA

$\mu_0$ (GPa)	H (GPa)	$\theta_0$ (K)	HP	g	$\hat{D}$ (MPa)
30.512	4.553	295.15	102.51	$7.682 \times 10^{-4}$	75.61
$k_1$ ( $m^{-1}$ )	$\dot{\varepsilon}_0$ ( $s^{-1}$ )	$\Delta F$ (eV)	$\Delta V$ ( $m^3$ )	E(MPa)	F(K)
81.24	$10^7$	1.326	$63.5b^3$	685	194

Table 3 Calibrated parameters of the crystal plasticity model for 22MnB5

$\mu_0$ (GPa)	H (GPa)	$\theta_0$ (K)	HP	g	$\bar{D}$ (MPa)
53.637	9.724	873.15	154.17	$3.077 \times 10^{-6}$	126.74
$k_1$ ( $m^{-1}$ )	$\dot{\epsilon}_0$ ( $s^{-1}$ )	$\Delta F$ (eV)	$\Delta V$ ( $m^3$ )	E(MPa)	F(K)
65.35	$10^7$	1.587	$80.33b^3$	536	241

Table 4 Error comparison between two-region and three-region methods in calibration

Temperature(AA)	300K	473K	623K	673K	723K	773K
3-region error (%)	6.98	4.61	6.37	5.88	6.94	4.58
2-region error	3.02	3.65	4.25	5.28	1.75	3.69
Temperature(BS)	873K	973K	1073K	1173K		
3-region error	10.41	8.56	7.46	9.28		
2-region error	6.53	5.25	7.16	7.67		

It is important to note that the above-mentioned process calibrates microscale material parameters defined at each material point of polycrystalline aggregate. Whereas experiments are performed at the macroscale and the overall behavior of the RVE characterize the damage evolution and mechanical behavior at plastic-deformation-dominated sites in the specimen. In view of the scale discrepancy and the large number of parameters to be calibrated using a relatively small set of experiments, the calibration process could result in non-unique set of parameters that accurately capture the experimental data. However, following the parameter calibration process, the previous identified parameters are checked to ensure that they are physically meaningful.

In order to further verify the model calibration for 7075 AA, the remaining curves of uniaxial tensile tests in Fig. 4(a) were simulated using CPFE and compared to the experimental data. All the simulation results are compared to experimental data in Fig. 16, which show a close agreement at different temperature conditions. The flow stress decreases when the temperature increases due to thermal softening of the local resistance in dislocation activation.

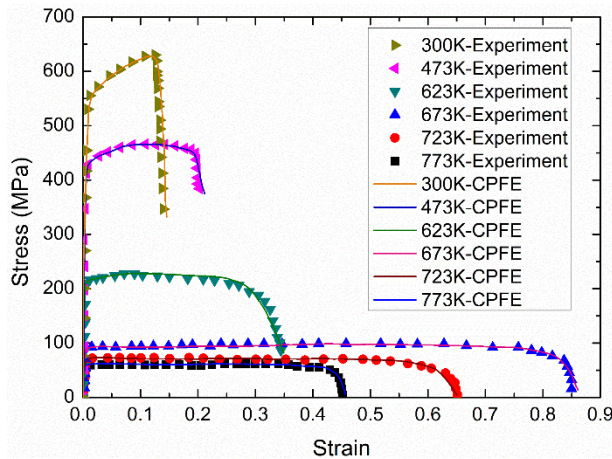


Fig. 16 Comparison between simulation of realistic tensile specimen and experimental data under different temperatures with stress-strain curves of 7075 AA.

The force-versus-displacement curves of shear tests at other temperatures are simulated for 22MnB5 with the calibrated parameters. During the entire loading process the shear specimen is at temperatures higher than 693K that is the martensite phase transition temperature. Thermal

softening also occurs for 22MnB5 BS and the thermal strain increases monotonically as temperature rises. The necking strain drop at high temperature range for 7075 AA is not observed in Fig. 17. In the CPFE simulation with different temperature conditions for 22MnB5 BS, the entropy term introduced previously remains negative for most of the grains. As temperature increases, the activation energy grows lower and the local shear strain becomes higher.

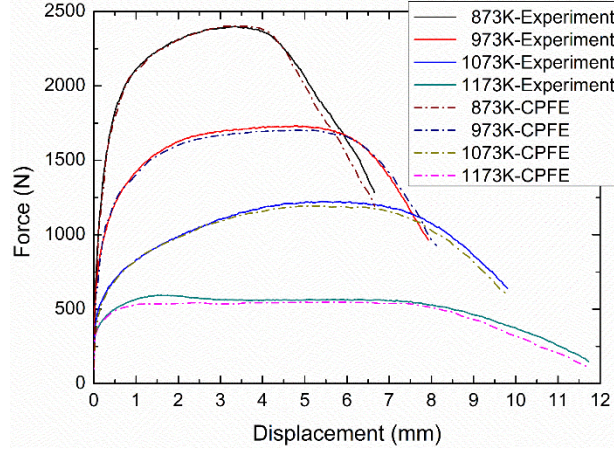


Fig. 17 Comparison between simulation of realistic shear specimen and experimental data under different temperatures with force-displacement curves of 22MnB5.

A key achievement of this work is that, using a single set of material parameters, model is able to achieve good agreement for all mechanical responses at all temperature conditions. Specifically, the hardening rates, damage softening, non-linear post-necking and fracture strain are simultaneously captured. In addition, the proposed model is confirmed as a useful tool for the similar cubic metals of FCC crystal in AA and BS at elevated temperatures. The good predictions of the tensile and shear mechanical behavior are the results of combination of three distinct mechanisms incorporated in the model. The thermal associated damage evolution, plastic dissipation and dislocation density based hardening mechanism are all activated in the simulations.

In this temperature-dependent CPFE simulation, the model is able to capture the fracture strain increase from 300K to 673K and its decrease from 673K to 773K. Necking softening occurs when strain reaches a critical value, defined as the critical necking strain, that differs in various temperature conditions. The maximum critical necking strain value is obtained at 673K. This indicates that this necking strain, does not have a linear correlation with temperature.

An entropy-like term is investigated to control the temperature-associated local shear strain and the corresponding critical necking strain. Extracted from the exponential function in Eq. (8),  $(\tau^\alpha \Delta V - s^\alpha \Delta V - \Delta F)/\theta$ , has the same unit of entropy. At low temperature range of 300K and 473K, the activation energy barrier is relatively high. The dislocation is hard to activate and escape from the obstacles. The entropy term is mostly negative in RVE and the local shear strain is low. At higher temperature of 623K and 673K, the activation energy is lower and more dislocations are nucleated and escape from the obstacles. The entropy term is still negative for nearly all the grains and the shear strain is higher as temperature increases. When temperature increases beyond 673K, the activation energy is still low. The dislocation pile-ups spread over the grains and generate high resistance for further dislocation activation in Eq. (13) and (14). The entropy term turns positive and the shear strain becomes lower as temperature increases.

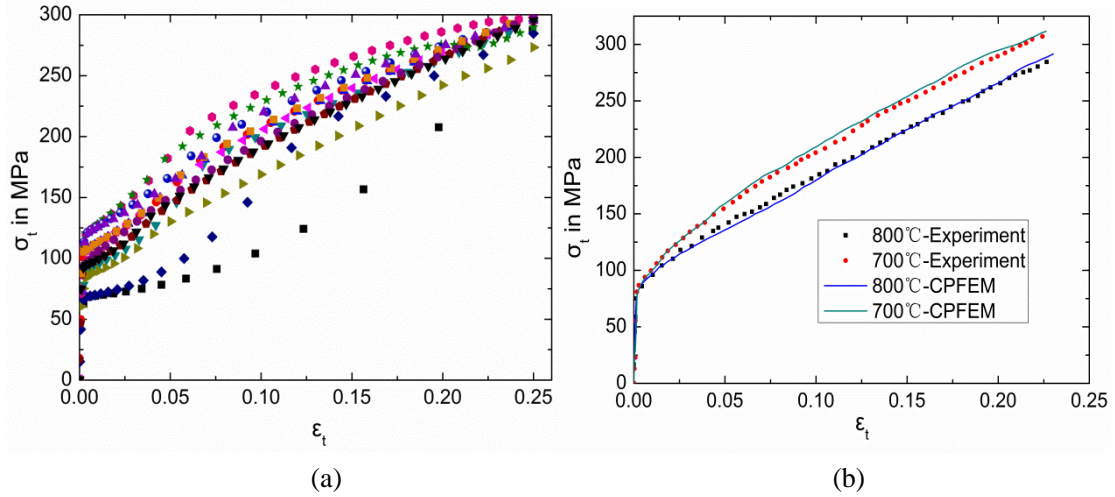


Fig. 18 CPFE simulation with temperature decreasing rate of  $33.6^{\circ}\text{C}/\text{s}$ : (a) 20 grains with different crystallographic orientations simulated in the tensile test with temperature drop. (b) Overall stress-strain curves in the CPFE simulation compared to the experimental data at two initial temperatures with strain rate of  $1 \times 10^{-3} \text{ s}^{-1}$ .

To cross validate the calibrated parameters in the temperature variation condition, the analyses of 22MnB5 tensile test is conducted. No damage evolution is considered in this case. In Fig. 18(a), results of 20 random grains in the simulation with temperature decreasing rate  $33.6^{\circ}\text{C}/\text{s}$  show the various microscopic mechanical behaviors at different crystallographic orientations of grains. The cooling rate is assumed to be uniform in the specimen. Using this CPFE model, RVE predictions of tensile mechanical behavior for 22MnB5 BS are performed at two initial temperatures  $700^{\circ}\text{C}$  and  $800^{\circ}\text{C}$  and the results agree well with the experimental data in Fig. 18(b). The nearly linear hardening tangent in the plastic region is captured by increasing elastic moduli in Eq. (12) and slip resistance in Eq. (9) in each grain of the RVE as temperature decreases.

## 6. Microstructural analyses of ductile fracture in shear and tensile test at high temperature

The calibrated CPFE-CDM models are used to perform specimen scale simulations of the shear and tensile experiments using hexahedral elements. The microstructural variables are analyzed to correlate with the void growth process and crucial microstructural metrics are determined on void nucleation and growth. Microscopic physical variables, including dislocation density, orientation mismatch and misorientation are studied in the necking region. The local dislocation density distribution is computed which is challenging to obtain with direct experimentation.

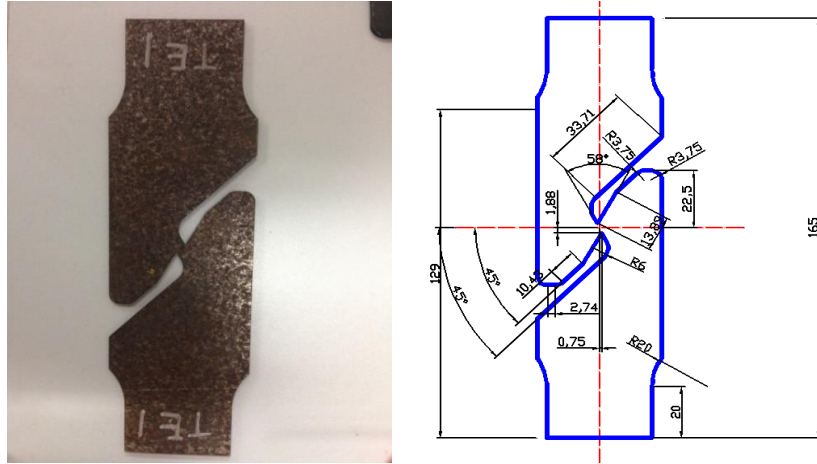


Fig. 19 The realistic specimen and the size marking in the wire-electrode cutting of specimen. The notch tip is treated as round to guarantee the pure shear behavior in the middle section.

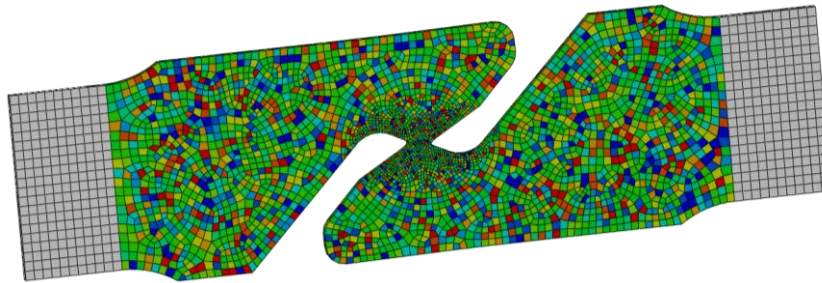


Fig. 20 The initial orientation distribution of  $\sin\theta \cdot \sin\varphi$  in shear specimen. The mesh in the middle section is refined.

### 6.1 Simulation of shear testing of 22MnB5 at 1173K

The realistic dimension measurement of the shear specimen is shown in Fig. 19, produced by wire-electrode cutting from a commercially produced 22MnB5 plate. The middle structure of this specimen ensures the pure shear at this stretching direction. In order to obtain accurate damage evolution response, small element size is specified in the middle section of the specimen. 7748 elements of C3D8 type is used in the shear simulation with full integration. The initial random grain orientation distribution in this shear specimen is shown in Fig. 20, by pre-defined orientation value of  $\sin\theta \cdot \sin\varphi$  in pole figure of Fig. 20(b) ( $\theta, \varphi, \psi$  are the Euler angles in Bunge's convention).



Fig. 21 Final fracture morphology in shear specimens of 22MnB5 steel at different temperatures

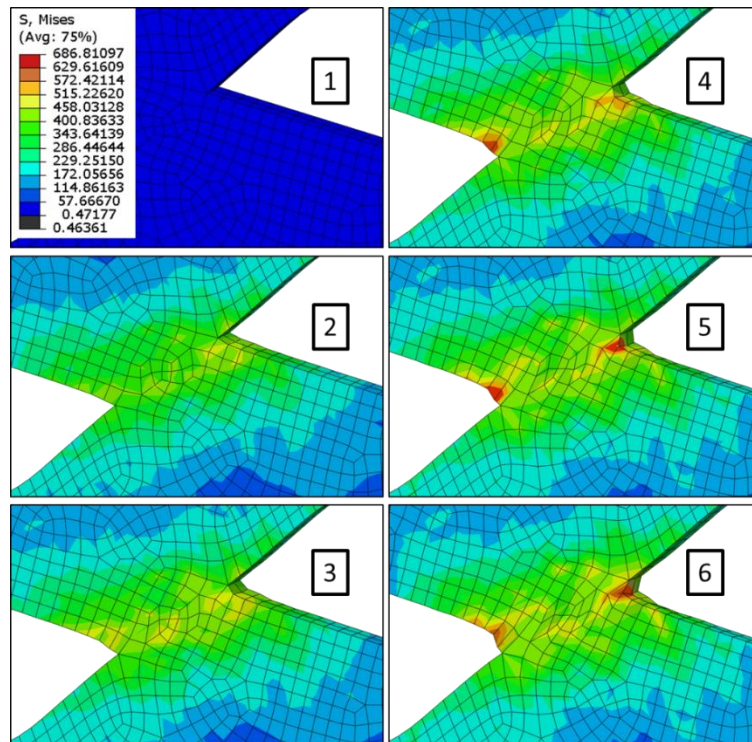


Fig. 22 Local stress distribution in the simulation of shear experiment of 22MnB5 boron steel at 1173 K. Number 1 to 6 are states at 0, 2, 4, 6, 8, 10 mm displacement, respectively.

Ultimate fracture morphologies for the thermal shear specimens are shown in Fig. 21 at different temperatures and the local deformation is presented at 1173 K. In thermal shear tests, two holes in the middle of the holder section are created to fit the stretcher and this nearly does not affect the shear fracture due to Saint-Venant's Principle. The ductile fracture is localized in the middle section. The ultimate fracture morphology of 22MnB5 BS is slightly different from that of other literature [85], which is mainly due to the different specimen geometry and the distinct material property.

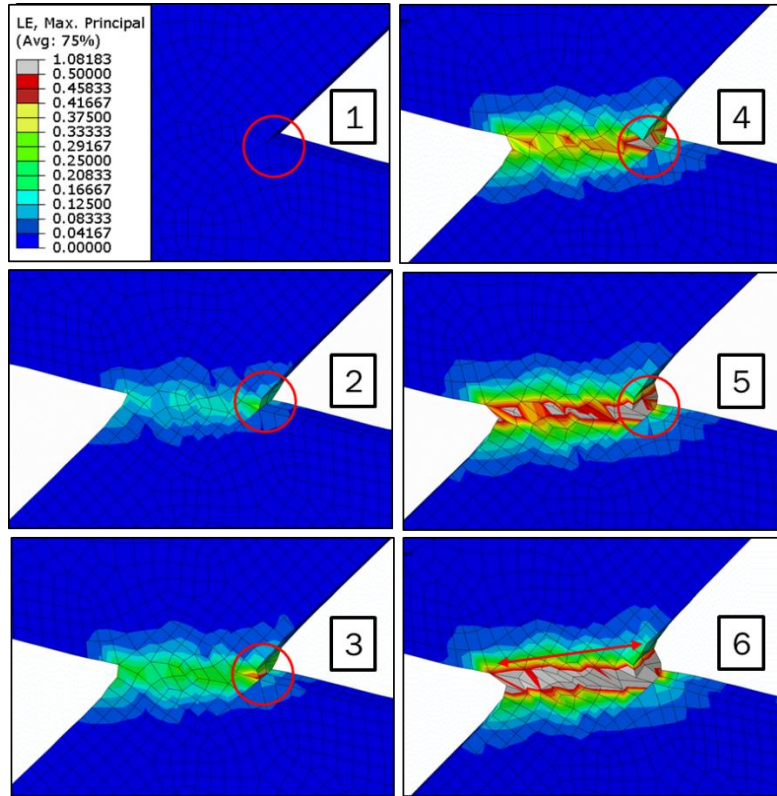


Fig. 23 Local strain distribution in simulation of 22MnB5 steel at 1173 K (arrow representing for the fracture direction and circle showing the position of severe deformation). Number 1 to 6 are states at 0, 2, 4, 6, 8, 10 mm displacement, respectively.

For shear test of 22MnB5 BS at 1173 K, simulation results of time-dependent stress and strain distributions are presented in Fig. 22 and Fig. 23, respectively. The displacement control is applied and the stress and strain levels in the holder section are much lower than that in the middle section. The logarithmic strain amplitude higher than 0.5 is shown in grey color in Fig. 23, which is compared to the void nucleation and growth patterns in Fig. 24. From the comparison, the correlation in local strain and damage distributions suggests that the void nucleation and growth occurs in the strain concentration sites due to localized plastic flow with the preferential dislocation slip. These two correlated strain and damage patterns are consistent with that in the recent literatures of ductile fracture [13,86–88].

Compared with local experimental fracture morphology in Fig. 25 at 1173K, the ultimate void distribution results show a fine prediction. From the consistent time-dependent distribution pattern in strain and damage evolution, it can be concluded that the void growth is promoted by local plastic flow, in agreement with the experimental view of Pineau et al, 2016. The elements near the notch tip region, circled in Fig. 23, experience high distortion and rotation. And the same severe plastic deformation is shown in Fig. 25. Moreover, the arrow in Fig. 23 and the damage propagation path in Fig. 24 show the similar ultimate shear fracture angle in Fig. 25.

In the time-dependent damage distribution in Fig. 24, the damage is initiated at the notch tips where high stress distribution occurs at the same spots. This phenomenon is consistent with the conclusion of Kim and Yoon, 2015 that local stress concentration was considered to trigger the damage initiation and evolution. It appears that stress distribution can be used to describe the

damage initiation pattern. However, the correlation between damage propagation path and stress concentration is not explicitly shown. The local stress distributions in Fig. 22(4) exhibit concentration patterns only at two notch tips as strain step increases, whereas damage grows and coalescences in the center of the damage region are shown in Fig. 24(6).

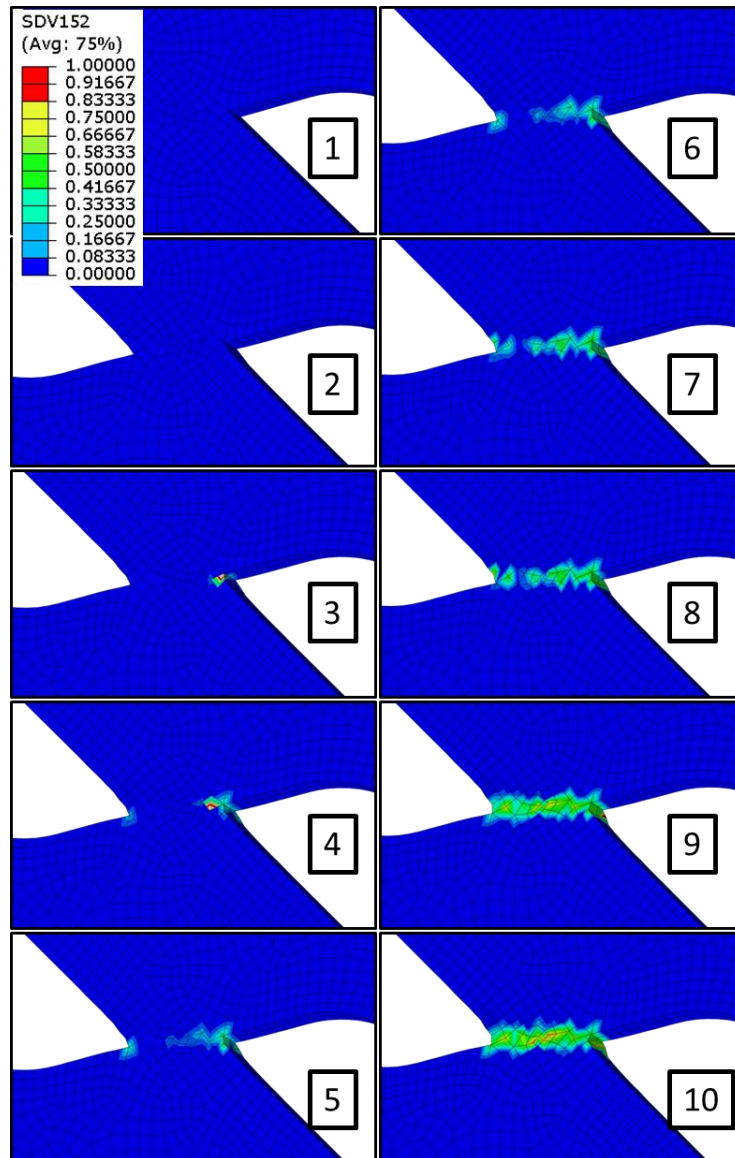


Fig. 24 Local damage evolution process in simulation of shear experiment of 22MnB5 boron steel in the middle section of specimen at 1173K. Number 1 to 10 are states at 0 to 10 mm displacement with 1 mm increment, respectively.

The damage and dislocation density are tracked throughout the shear specimen. Coupling with dislocation density in this study, the interaction between dislocation flux and grain boundary is explicitly shown using dislocation density distribution. To further study the correlation between microstructural variables and damage initiation, local stress and dislocation density distributions are investigated along the damage propagation line. In Fig. 26, the magnitudes of these two variables are plotted in each individual element in normalized position, when local damage initiates at notch tips of the specimen ( $D^{\alpha} \geq 0$  at the notch tip). The maximum values of both variables are distributed near the damage initiation spots. From this perspective, the stress and dislocation density

distributions are strongly linked to damage initiation and could be used to predict spatial damage initiation sites.



Fig. 25 The experiment of the local middle part of the 22MnB5 specimen at 1173 K (arrow representing for the fracture direction and the circle showing the position of severe deformation)

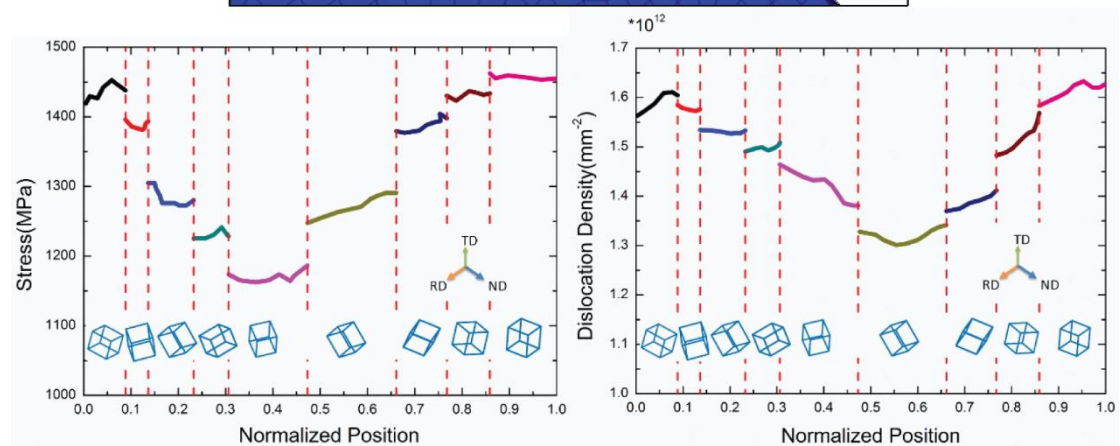
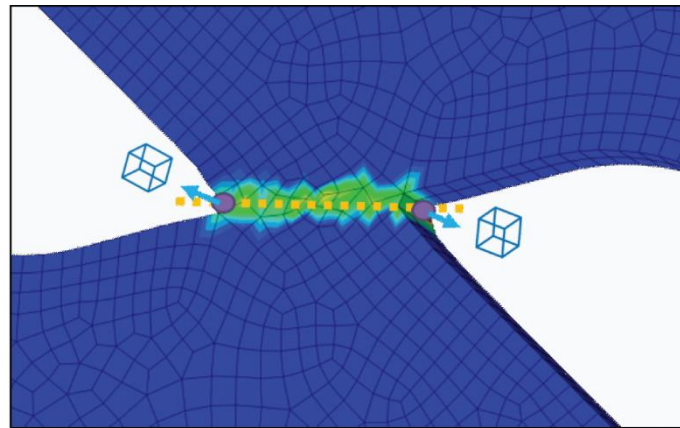


Fig. 26 The local Mises stress and dislocation density distributions through specific line along necking path when local damage begins to initiate ( $D^{\alpha} \geq 0$ ) at notch tip for 22MnB5 at 1173 K. Normalized positions from 0.0 to 1.0 represent grain sites from left to right in the line.

In Fig. 26, the dislocation pile-ups and stress concentrations occur both inside each individual grain and on the grain boundary. This implies that dislocation flow could be blocked inside grain by substructures and dislocations pile up at grain substructure and grain boundary. Void growth induced by preferential dislocation slip could result in both transgranular and intergranular damage. This prediction of damage mechanism needs further experimental investigation for 22MnB5 BS at

elevated temperatures to obtain fully austenitized grains. High temperature EBSD combined with SEM could be applied for understanding the physical damage mechanism at grain scale.

The stress distribution along normalized position is very non-uniform due to orientation mismatch between adjacent grains. When crystallographic orientation differed severely between two grains, the stress amplitudes separate at grain boundaries. The separation of dislocation density level is relatively mild and the discontinuities of dislocation density level at grain boundary is smaller. This results from different resolved shear stress level between adjacent grains with different orientations. In addition, the dislocation penetrating flow through grain boundary results in relatively low dislocation density jump at the grain interface.

## **6.2 Simulation of tensile testing of 7075 AA at 473K**

Tensile numerical simulation analysis is performed to investigate damage evolution in the 7075AA specimens subjected to tensile loading. In this simulation, 8880 elements of C3D8 type mesh are used with full integration. The evolution of principal strain and damage distributions at 473K throughout the specimen are presented in Fig. 27 and 28, respectively.

Consistent distributions in Fig. 27 and 28 indicates that the high damage sites follow the strain concentration spots in the necking region, which is similar to previous phenomenon in shear test of 22MnB5 BS. This observation proves that the void initiation and growth in FCC material have a strong correlation with local strain. Phenomenological macroscale strain-associated damage models are employed to model the similar relationship [15,89].

Through a specific line along the damage localization zone (i.e., the necking area), local stress and dislocation density distributions are shown in Fig. 29 when damage initiates ( $D^{\alpha} \geq 0$  at the middle spot). The maximum stress and dislocation density magnitude are in the same grain and its lattice orientation is pointed out in Fig. 29. From previous analysis in 22MnB5, stress concentration and high dislocation pile-ups are considered as the indicator of damage initiation. The severe orientation mismatches between adjacent lattices results in relatively high dislocation density and high stress level near the grain boundary, which is consistent with ref. [14] that the stress concentration results from the orientation mismatch near grain boundaries for AA. Thus, it can be concluded that damage nucleates first near the middle spot in the specimen and the dislocation density is considered as the necessary variable for damage activation. Above all, dislocation density in this model is proved as the indicator for predicting local damage initiation sites in FCC material at elevated temperatures.

Different from dislocation density distribution in 22MnB5 BS, the high dislocation density spots in Fig. 29 tend to locate at the grain boundary and severe orientation mismatches are observed in adjacent grain pairs. It implies that the grain boundary in 7075 AA, rather than the grain substructure, generates the main resistance for dislocation flow. Void growth for ductile fracture is aided by the dislocation pile-ups at the grain boundary. In this case, intergranular damage may be the predominant local fracture mode occurring in these boundaries at elevated temperature, which is consistent with previous experimental observation in Section 2.

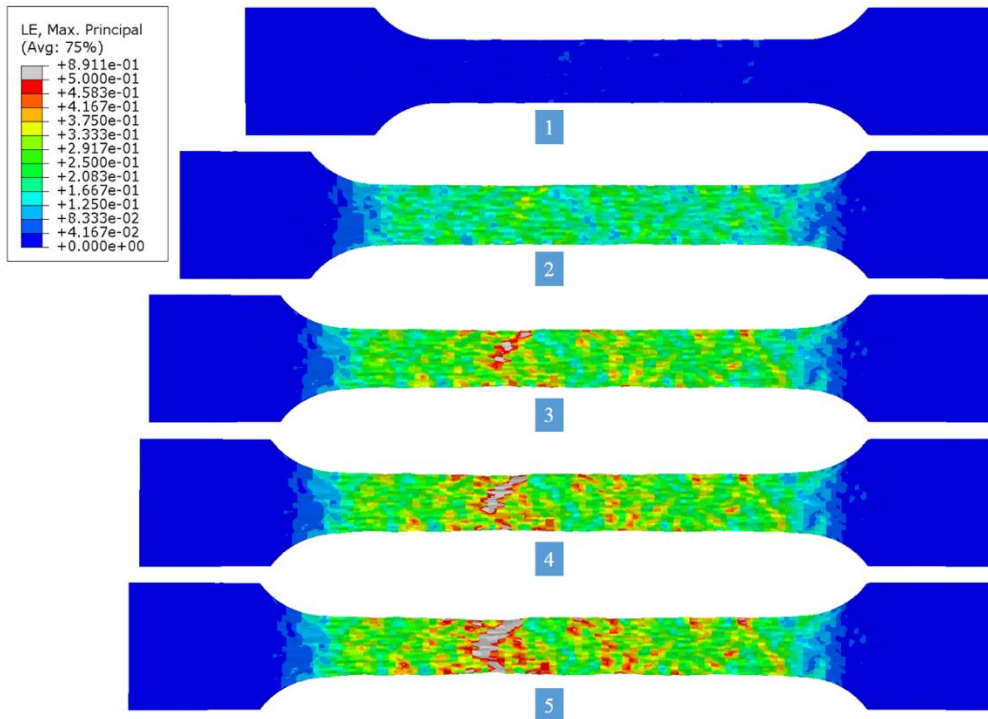


Fig. 27 Strain distribution of the tensile experiment of the 7075 AA in CPFE simulation at 473 K. Indexes from 1 to 5 means total accumulated strain value of 0.011, 0.087, 0.141, 0.161, and 0.187.

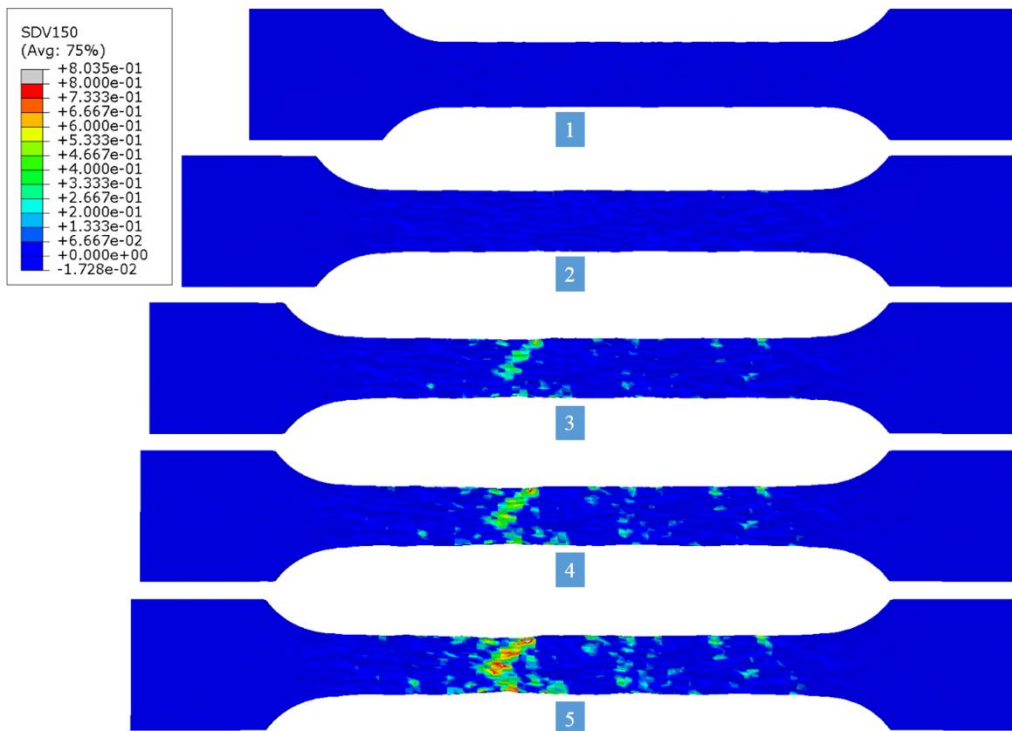


Fig. 28 Damage distribution of tensile experiment of the 7075 AA in CPFE simulation at 473 K. Indexes from 1 to 5 means total accumulated strain value of 0.011, 0.087, 0.141, 0.161, and 0.187.

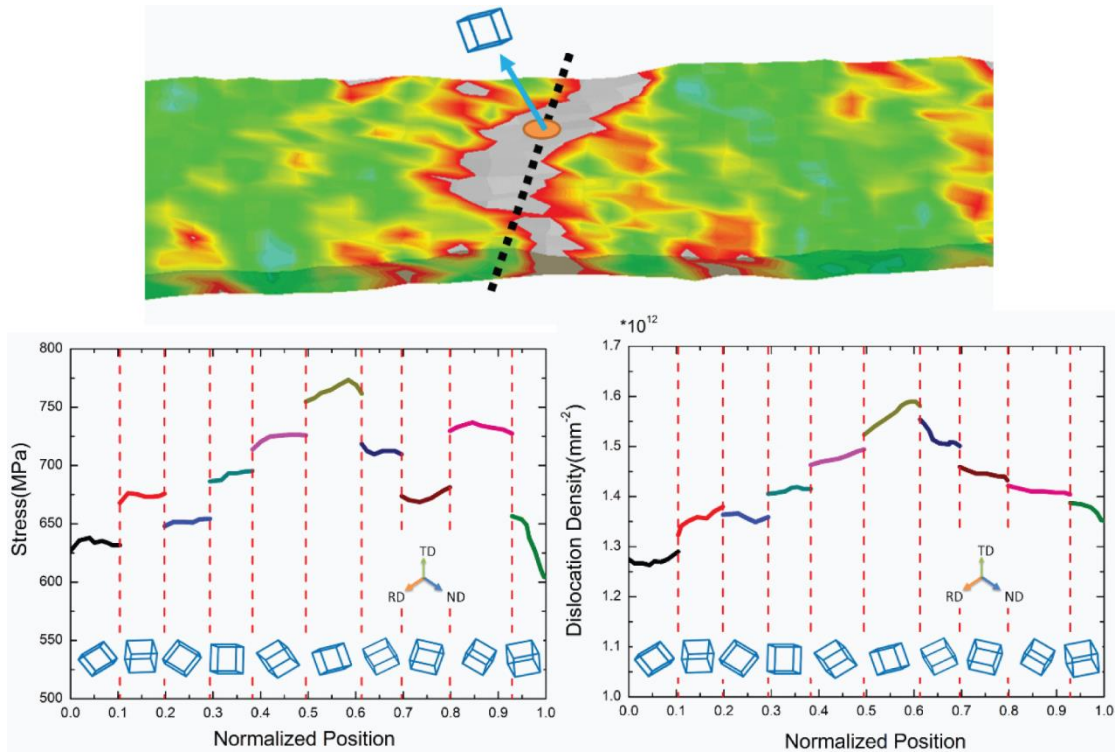


Fig. 29 The stress and dislocation density distribution through specific line along necking path when  $D^\alpha \geq 0$  over the entire specimen for 7075 AA tensile test at 473 K. Normalized positions from 0.0 to 1.0 represent grain sites from bottom to top in the line. Grey color represents the logarithmic strain higher than 0.5 compared with damage distribution.

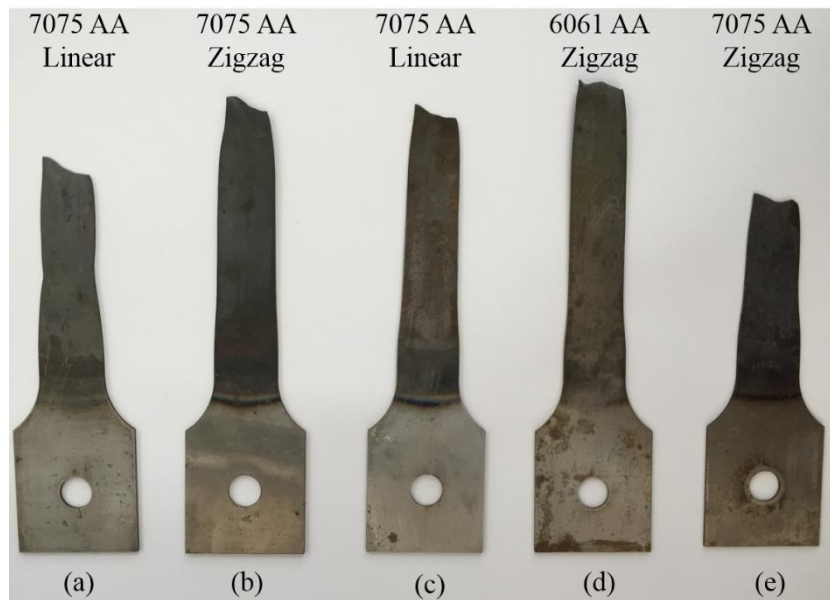


Fig. 30 Different fracture morphologies of 7075 and 6061 AA in thermal tensile test at 473K.

To better understand the mechanism of plasticity-aid void nucleation and growth, the relationship between microstructural variables and void growth path (necking path) is discussed. It has been discussed in Section 5.2 that the void growth path in this study is strongly influenced by the microscale preferential dislocation slip. In tensile test of AA, local crystallographic orientations at

the identical locations of two same-geometry specimens are different. Accordingly, distinct damage coalescence paths are observed that generate different fracture morphologies in Fig. 30.

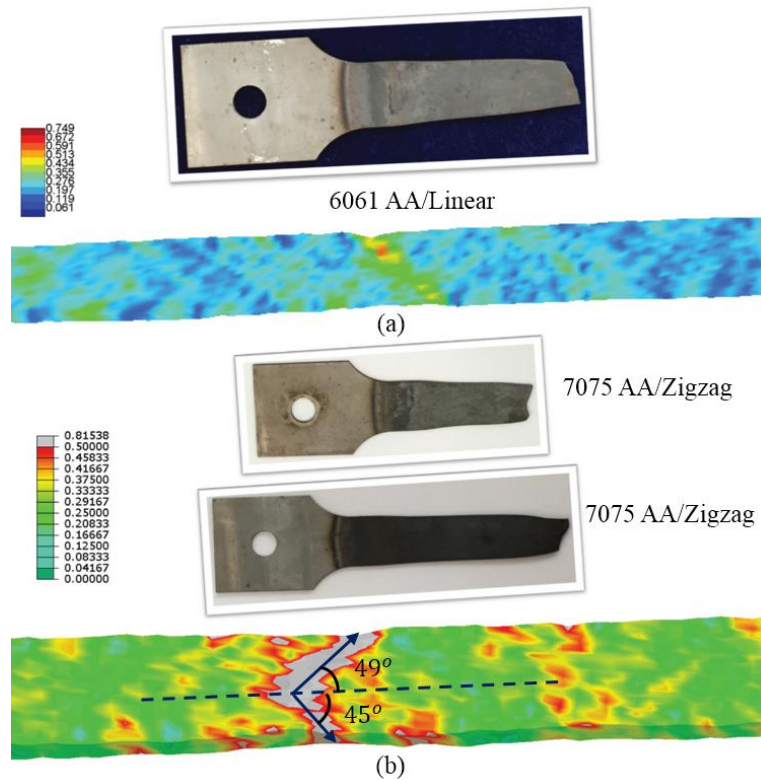


Fig. 31 The necking patterns (principal strain distributions) in CPFЕ simulations compared to fracture morphologies of actual specimens: (a) 6061 AA (473K); (b) 7075 AA (473K)

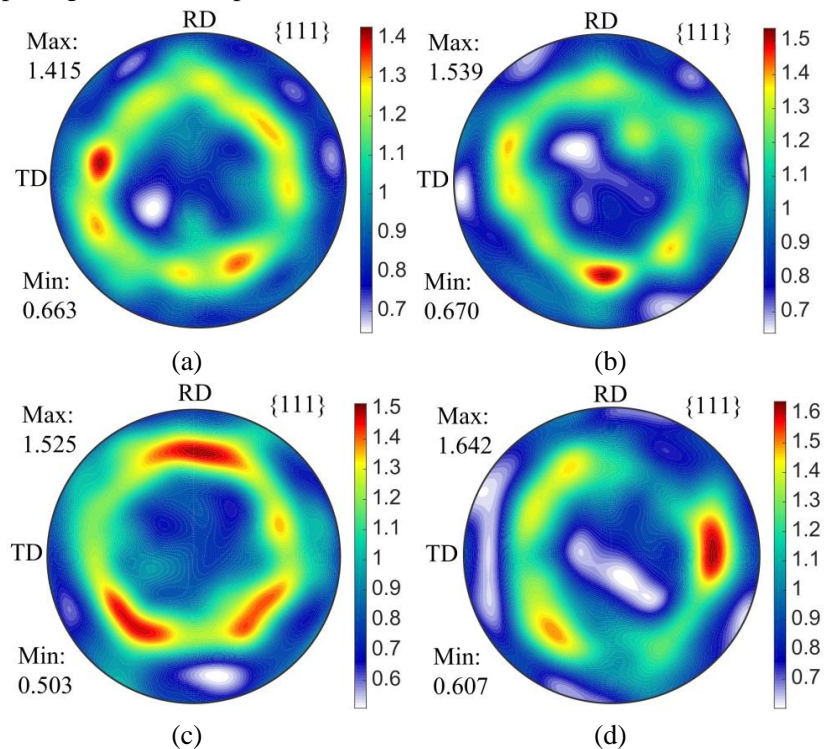


Fig. 32 Pole figure of density of orientation distribution: (a) undeformed 6061AA (b) deformed 6061AA (473K, predicted) (c) undeformed 7075AA (d) deformed 7075AA (473K, predicted)

At 473K, the same tensile test is applied for 6061 AA and 7075 AA with the wire-cut specimen of same geometry. Two fracture morphologies are obtained including zigzag and linear fracture modes in Fig. 31. The linear mode of 6061 AA has already been captured by the previous phenomenological CPFEM model [53]. Whereas the zigzag mode of 7075 AA is well described by the strain localization and void growth path in the current model. In Fig. 31(a), the strain concentration of 6061 AA is initiated at the two edges of the specimen where necking begins and the shear band spreads across the specimen until the material separation happens across the single shear band [53]. A different strain, or void growth pattern is observed for 7075 AA in Fig. 31(b). Shown in Fig. 27 and 28, the void growth is first observed at both the middle and edge spots. Two localized shear bands extend in two directions and intersect at the middle spot. Subsequently, the void growth along the shear band and zigzag necking path is generated. The zigzag fracture mode forms when material separate through the necking path.

In FCC materials, microstructure is determined to have important influence on the necking path [14,90]. Various features of microstructure are discussed but the predominant factor is not determined for forming the observed distinct necking modes. In the following study, multiple characteristic crystallographic variables including texture evolution, orientation distribution, local misorientation angles and Schmid factors are analyzed to determine the key microstructural effect on the damage initiation, void growth and necking path.

For 6061 and 7075 AA, the localized dislocation behavior is determined by the crystallographic orientation of individual grains. Here, the numerically predicted deformed pole figures in these two microstructures are presented in Fig. 32. Due to large deformation and lattice reorientation at 473K, volume fraction of specific grain orientation tends to increase as significant localized plastic deformation occurs. In Fig. 32, the density of crystallographic orientation  $\{111\}[\bar{1}\bar{1}1]$  increases in 7075 AA after the tensile test. Whereas in study of 6061 AA, the density of estimated orientation  $\{111\}[100]$  rises. However, the density rise is not significant in both materials and the relation between grain reorientation and localized plastic flow is not explicit in this case.

In 6061 AA of FCC crystal structure, the cross section of tensile specimen contains relatively large grains [53]. As for 7075 AA, the average grain size and the transverse geometric dimension are about 103.4  $\mu\text{m}$  and 12.5mm, respectively. This means that only about 121 grains lie through the width length of the experimental specimen. Since the specimen width is small, limited grains are observed through cross section for 6061AA and 7075 AA. Each individual grain has an important effect on the local preferential dislocation flux and damage evolution. Thus, the initial misorientation distribution have a significant influence on the local preferential dislocation activation and it is investigated to correlate with void growth path.

In order to analyze only the effect of initial misorientation distribution on necking path observed in Fig. 32, instead of considering the effect from material property, we utilize the identical mesh for the two specimens and map the same orientation distribution function (ODF) of 7075 AA onto 6061 AA specimen. It should be noted that the initial specimen sizes of 6061 AA and 7075 AA are the same. The principal strain distribution of 6061 AA in Fig. 33 is obtained in uniaxial loading at 473K, which has the almost same zigzag fracture morphology but different strain magnitude compared with zigzag result of 7075 AA in Fig. 30(b). The necking angles of 6061 AA with orientation mapping are about 48° (upper) and 44° (lower), which are the similar with 49° (upper) and 45° (lower) in 7075 AA. From this analysis, it can be concluded that identical mapping of initial

ODF leads to similar dislocation nucleation sites and almost the same necking path. In addition, the initial misorientation distribution has an important effect on localized plastic flow and the corresponding void growth path for AA at high temperature conditions. The declining grain reorientation at elevated temperatures in these two AA enhance the similarity of the necking path between Fig. 31(b) and 33.

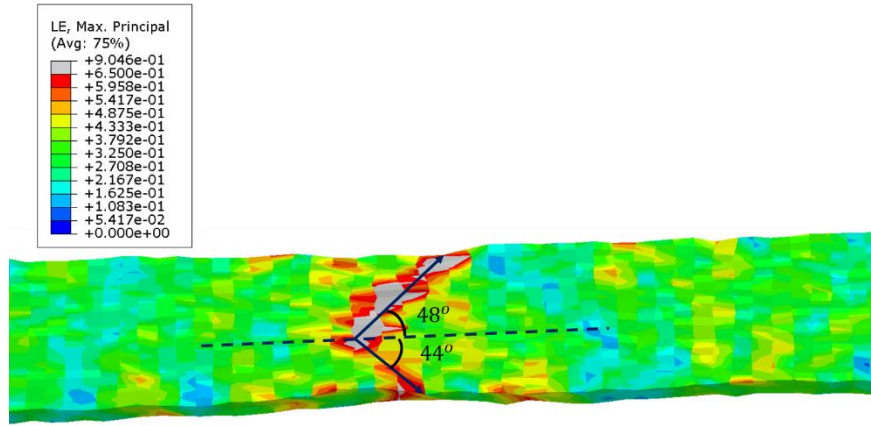


Fig. 33 Principal strain distribution in thermal tensile simulation of 6061 AA (473K) using exact mapping of ODF from 7075 AA (same mesh geometry and specimen size).

To predict the damage initiation sites, the local mismatch and misorientation distribution are analyzed statistically in connection with damage variable near necking paths. In the crystallographic aspect, the orientation mismatch which causes strain heterogeneity across grain boundary is an essential effect in predicting damage initiation sites. Since local orientation mismatches are tightly linked to strain localization and corresponding void growth, it is worth investigating the correlation between necking paths and misorientation angles of local grain pairs.

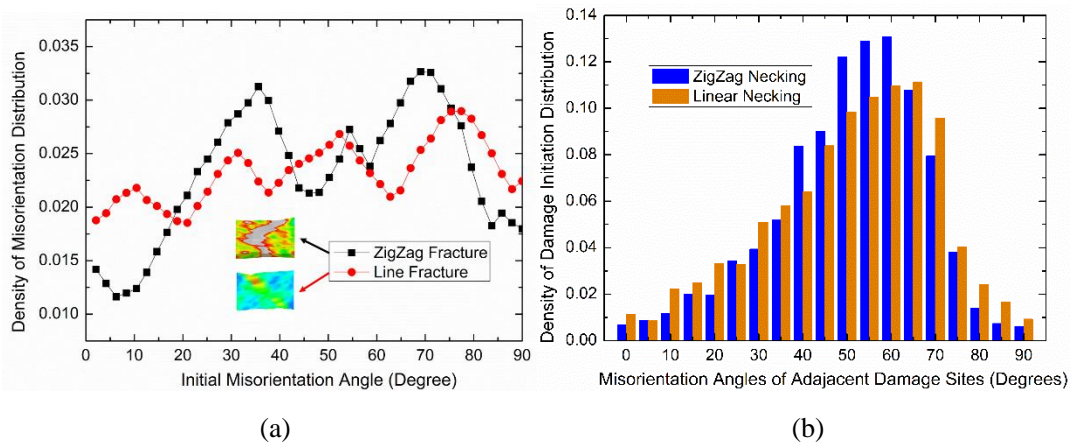


Fig. 34 Two misorientation study for 6061 AA of line fracture and 7075AA of zigzag fracture at 473K. (a) Initial misorientation distribution in the tensile specimen; (b) Density of damage initiation sites within 5-degree misorientation angle ranges at the total deformation  $\epsilon = 0.157$

The misorientation distribution patterns of 6061 AA (473K, linear necking) and 7075 AA (473K, zigzag necking) are computed in Fig. 34(a). This proves that possible void nucleation and growth are sensitive to local orientation mismatch, which is consistent with experimental observations [91]. On the purpose of quantifying this correlation and eliminating the effect of material property in

dislocation activation, the two misorientation distribution patterns are both calculated for 7075 AA in the current CPFEE framework.

In the CPFEE analysis of 7075 AA at 473K, total deformation  $\epsilon = 0.157$  is specified in the strain hardening region as the damage variable  $D^\alpha > 0$  occurs at multiple sites for different necking morphologies. These sites are considered as the potential void growth sites. 347 and 325 void growth sites are collected for zigzag and linear necking, respectively. 83.4% and 82.2% void growth sites are obtained along the necking region, which proves that necking region has higher potential in promoting void growth. The orientation mismatches between two adjacent sites are collected. The angles are grouped into boxes of 5 degree and plotted for the possible void growth sites in Fig. 34(b).

Results in Fig. 34(b) shows that the high possibility to find void growth sites at the critical misorientation angle range from  $50^\circ$  to  $65^\circ$  in the zigzag necking behavior whereas  $60^\circ$  to  $75^\circ$  in the linear necking behavior. It implies that the dislocation pile-ups and grain interactions are more intense at these grain pairs. Furthermore, the intergranular crack has the higher potential to occur at the adjacent grains with these specific mismatch angles in the necking area. Too high or too low misorientation angles are less susceptible to void growth. In both necking cases, the orientation mismatch lower than  $50^\circ$  or higher than  $75^\circ$  are considered not possible for void growth. High interfacial strength of the grain pairs is the main reason for these misorientation angles.

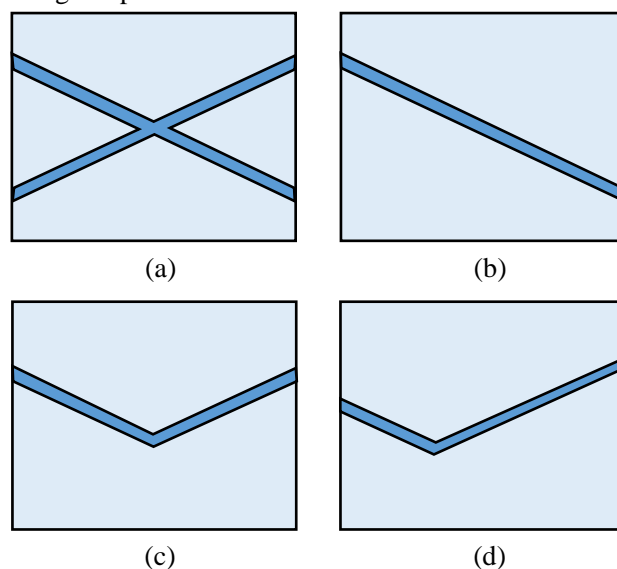


Fig. 35 For random misorientation distributions in the simulation, the schematic shear bands in the necking region for 7075 (473K) tensile specimen: (a) ideal shear bands; (b) linear necking; (c) zigzag necking; (d) deviated zigzag necking.

To understand the misorientation dependence for different necking modes, random misorientation distributions are generated and misorientations in the necking regions are investigated for 7075AA tensile tests. The schematic fracture morphologies for these simulations are presented in Fig. 35 (b), (c) and (d), including three types, linear necking, zigzag necking and deviated zigzag necking. In the numerical simulation, the localized ideal shear bands in Fig. 35 (a) occur in strain hardening region. Multiple shear bands are generated by local plastic deformation. As plastic deformation becomes severe, the shear bands begin to collapse into a localized one at the onset of necking behavior. The collapsing necking path is mainly influenced by the dislocation pile-ups in the local region where local mismatch angles reach the critical mismatch range. Whereas, the zigzag or

deviated zigzag necking would be arrested at local site when its misorientation angle exceeds the critical mismatch angle. The phenomenon is consistent with the experimental observations that the zigzag or linear necking behavior occurs due to localized plastic shear bands from severe dislocation activation. And material separation or crack propagation would take place along these necking regions through shear bands [29].

Table 5 At total deformation  $\epsilon = 0.165, 0.174$ , maximum and minimum value of local mismatch angles and Schmid factors at damage initiation sites in subsequent necking region using three random misorientation distribution functions (MODF) for 7075 AA (473K).

Value	Mismatch (degree)		Schmid Factor	
	min	max	min	max
MODF 1	53.83	67.87	0.25	0.42
MODF 2	63.42	77.31	0.37	0.41
MODF 3	58.25	74.74	0.38	0.46

For numerical verification of the obtained critical orientation mismatch range for void growth, at total deformation  $\epsilon = 0.165, 0.174$ , the mismatch angles of possible adjacent void growth sites in the subsequent necking region are presented for three random misorientation distribution functions (MODFs) in Tab. 3. The results show that more than the misorientation of previous potential void growth sites outside the necking path exceeds or near the edge of the critical range  $[50^\circ, 75^\circ]$ . At these sites, the damage variables stop increasing and the void growth is arrested. When total deformation reaches  $\epsilon = 0.165, 0.174$ , the mismatch angles along the necking region are increased to 85.0%, 87.1% and 84.3%, 86.8% for zigzag and linear necking path, respectively. And the angles are mostly inside or near the critical range. The Schmid factors are also presented for the possible void growth sites in the subsequent necking area in Tab. 3. Higher Schmid factor are correlated with the higher local resolved shear stress and intense slip rate in the local grain. Previous study of AA at room temperature shows that local grains oriented preferential for slip could induce damage initiation [54,92–94]. In this study, the preferential slip with relative high Schmid factor range of 0.35 to 0.5 is observed in the damage initiation region. However, low value of 0.25 is also collected in the adjacent sites with maximum damage  $D^\alpha$  of 0.53. This implies that the individual grain orientation with high Schmid factor is not necessary to trigger void growth. The void growth under thermo-mechanical loading is more sensitive to local orientation mismatch.

## 7. Discussion and Conclusion

The proposed micro-damage model integrated with the effect of by local dislocation mobility on void nucleation and growth on an experimental basis. This approach shows reasonable results for two face-centered cubic polycrystalline materials at high temperature ranges. At quasi-static range, shear-dominated and tensile tests are performed and no dynamic strain aging is observed here. It appears to be impossible to perform the thermal real-time EBSD scan to study the microstructure evolution in thermo-mechanical behavior, thus the computational investigation is implemented by incorporating dislocation density based crystal plasticity combined the damage model. The fracture strain and critical necking strain are captured well by this model. A crack length and void embedded model is expected to model the void coalescence and crack initiation [95,96] and to answer the fundamental question of dominated mode in ductile fracture [29,97].

In practical engineering application, the proposed model could be inefficient since the two-way

coupling of full temperature field and mechanical field is applied. It is worth noting that the proposed method is mesh-dependent and critical mesh size of 1.5 times average grain size is deduced as the previous manner [53] that reaches convergence. In the future study, homogenization methods could be applied to simulate large-scale structural components coupling with crystal plasticity or thermo-mechanics [98,99].

At various elevated temperatures, the shear and tensile experiments are performed for 7075 AA and 22MnB5 BS respectively to investigate ductile fracture under high temperature conditions. Shear-dominated and tensile specimens are designed and aligned in the horizontal direction for thermo-mechanical experiments at quasi-static strain rates.

A crystal plasticity model CPFEM-CDM is proposed which incorporates rate- and temperature dependency, dislocation-density-based strain hardening and microscale damage evolution. The dislocation density, temperature and damage are treated as internal variables and account for the thermal- and damage softening in crystal plasticity framework. Reasonable prediction is obtained between simulation and experimental results for different specimens, temperatures and materials. Specifically, hardening rates, post-necking and fracture strain are captured for all temperature conditions using a single calibrated set of parameters for one material. The critical thermal necking strain is found to be influenced by an entropy-like term in the thermal activation mechanism.

Computational analysis of microstructural effects on ductile fracture is conducted at the necking region regarding variables of crystallographic orientation and dislocation density. Dislocation density distribution is computed and associated with damage initiation sites which indicate the possible damage modes of transgranular and intergranular damage. Multiple fracture morphologies in tensile test of 7075 AA is computed and related with initial orientation distribution. To predict the potential void growth sites, critical orientation mismatch ranges are computed for both zigzag and linear necking shapes and the void growth of the critical range is verified at high strain.

## Acknowledgements

This work was funded by the Key Project of the National Natural Science Foundation of China (No.11272075), China Postdoctoral Science Foundation (2014M561223), the Fundamental Research Funds for the Central Universities (DUT14RC(3)032) and the financial support from the program of China Scholarships Council (No. 201606060105).

## Data Availability

The datasets generated and/or analysed during the current study are available from the corresponding author on reasonable request.

## References

- [1] H. Karbasian, A.E. Tekkaya, A review on hot stamping, *J. Mater. Process. Technol.* 210 (2010) 2103–2118. doi:10.1016/j.jmatprotec.2010.07.019.
- [2] S. Toros, F. Ozturk, I. Kacar, Review of warm forming of aluminum-magnesium alloys, *J. Mater. Process. Technol.* 207 (2008) 1–12. doi:10.1016/j.jmatprotec.2008.03.057.
- [3] M. Merklein, M. Wieland, M. Lechner, S. Bruschi, A. Ghiotti, Hot stamping of boron steel sheets with tailored properties: A review, *J. Mater. Process. Technol.* 228 (2016) 11–24. doi:10.1016/j.jmatprotec.2015.09.023.
- [4] K. Alharbi, H. Ghadbeigi, P. Efthymiadis, M. Zanganeh, S. Celotto, R. Dashwood, C. Pinna,

- Damage in dual phase steel DP1000 investigated using digital image correlation and microstructure simulation, *Model. Simul. Mater. Sci. Eng.* 23 (2015). doi:10.1088/0965-0393/23/8/085005.
- [5] K.O. Pedersen, I. Westermann, T. Furu, T. Børvik, O.S. Hopperstad, Influence of microstructure on work-hardening and ductile fracture of aluminium alloys, *Mater. Des.* 70 (2015) 31–44. doi:10.1016/j.matdes.2014.12.035.
- [6] A.S. Khan, S. Yu, H. Liu, Deformation induced anisotropic responses of Ti-6Al-4V alloy Part II: A strain rate and temperature dependent anisotropic yield criterion, *Int. J. Plast.* 38 (2012) 1–13. doi:10.1016/j.ijplas.2012.03.013.
- [7] F. Kabirian, A.S. Khan, A. Pandey, Negative to positive strain rate sensitivity in 5xxx series aluminum alloys: Experiment and constitutive modeling, *Int. J. Plast.* 55 (2014) 232–246. doi:10.1016/j.ijplas.2013.11.001.
- [8] L. Chen, G. Zhao, J. Yu, W. Zhang, Constitutive analysis of homogenized 7005 aluminum alloy at evaluated temperature for extrusion process, *Mater. Des.* 66 (2015) 129–136. doi:10.1016/j.matdes.2014.10.045.
- [9] L. Chen, J. Chen, R.A. Lebensohn, Y.Z. Ji, T.W. Heo, S. Bhattacharyya, K. Chang, S. Mathaudhu, Z.K. Liu, L.Q. Chen, An integrated fast Fourier transform-based phase-field and crystal plasticity approach to model recrystallization of three dimensional polycrystals, *Comput. Methods Appl. Mech. Eng.* 285 (2015) 829–848. doi:10.1016/j.cma.2014.12.007.
- [10] T.K. Eller, L. Greve, M.T. Andres, M. Medricky, A. Hatscher, V.T. Meinders, A.H. Van Den Boogaard, Plasticity and fracture modeling of quench-hardenable boron steel with tailored properties, *J. Mater. Process. Technol.* 214 (2014) 1211–1227. doi:10.1016/j.jmatprotec.2013.12.015.
- [11] D. Zhao, Y. Zhu, L. Ying, P. Hu, Y. Chang, W. Zhang, Numerical simulation of deformation behavior of 22MnB5 boron steel at elevated temperatures and experimental verification, *Acta Mech. Solida Sin.* 27 (2014) 579–587. doi:10.1016/S0894-9166(15)60003-9.
- [12] J. Zhou, B. Wang, M. Huang, Two constitutive descriptions of boron steel 22MnB5 at high temperature, *Mater. Des.* 63 (2014) 738–748. doi:10.1016/j.matdes.2014.07.008.
- [13] C.C. Tasan, J.P.M. Hoefnagels, M. Diehl, D. Yan, F. Roters, D. Raabe, Strain localization and damage in dual phase steels investigated by coupled in-situ deformation experiments and crystal plasticity simulations, *Int. J. Plast.* 63 (2014) 198–210. doi:10.1016/j.ijplas.2014.06.004.
- [14] J.B. Kim, J.W. Yoon, Necking behavior of AA 6022-T4 based on the crystal plasticity and damage models, *Int. J. Plast.* 73 (2015) 3–23. doi:10.1016/j.ijplas.2015.06.013.
- [15] J.Q. Tan, M. Zhan, S. Liu, T. Huang, J. Guo, H. Yang, A modified Johnson-Cook model for tensile flow behaviors of 7050-T7451 aluminum alloy at high strain rates, *Mater. Sci. Eng. A.* 631 (2015) 214–219. doi:10.1016/j.msea.2015.02.010.
- [16] K. Hagihara, T. Mayama, M. Honnami, M. Yamasaki, H. Izuno, T. Okamoto, T. Ohashi, T. Nakano, Y. Kawamura, Orientation dependence of the deformation kink band formation behavior in Zn single crystal, *Int. J. Plast.* 77 (2016) 174–191. doi:10.1016/j.ijplas.2015.10.005.
- [17] B. Klusemann, G. Fischer, T. Böhle, B. Svendsen, Thermomechanical characterization of Portevin-Le Châtelier bands in AlMg3 (AA5754) and modeling based on a modified Estrin-McCormick approach, *Int. J. Plast.* 67 (2015) 192–216. doi:10.1016/j.ijplas.2014.10.011.
- [18] H. Abdolvand, M. Majkut, J. Oddershede, S. Schmidt, U. Lienert, B.J. Diak, P.J. Withers, M.R. Daymond, On the deformation twinning of Mg AZ31B: A three-dimensional synchrotron X-ray

- diffraction experiment and crystal plasticity finite element model, *Int. J. Plast.* 70 (2015) 77–97. doi:10.1016/j.ijplas.2015.03.001.
- [19] W. Muhammad, B.A. P., J. Kang, M.R. K., I. Kaan, Experimental and numerical investigation of texture evolution and the effects of intragranular backstresses in aluminum alloys subjected to large strain cyclic simple shear, *Int. J. Plast.* Accepted (2016) 1–27. doi:10.1016/j.ijplas.2016.11.003.
- [20] S.H. Choi, D.W. Kim, B.S. Seong, A.D. Rollett, 3-D simulation of spatial stress distribution in an AZ31 Mg alloy sheet under in-plane compression, *Int. J. Plast.* 27 (2011) 1702–1720. doi:10.1016/j.ijplas.2011.05.014.
- [21] C. Keller, E. Hug, A.M. Habraken, L. Duchêne, Effect of stress path on the miniaturization size effect for nickel polycrystals, *Int. J. Plast.* 64 (2015) 26–39. doi:10.1016/j.ijplas.2014.07.001.
- [22] P. Hu, D. Shi, L. Ying, G. Shen, W. Liu, The finite element analysis of ductile damage during hot stamping of 22MnB5 steel, *Mater. Des.* 69 (2015) 141–152. doi:10.1016/j.matdes.2014.12.044.
- [23] J. Zhang, Y. Liu, J. Liu, Y. Yu, S. Wang, The effect of Gd element and solution treatment on the microstructure of AZ31 magnesium alloy and its kinetic model, *J. Alloys Compd.* 663 (2016) 610–616. doi:10.1016/j.jallcom.2015.12.133.
- [24] X. Zhang, C. Oskay, Polycrystal plasticity modeling of nickel-based superalloy in 617 subjected to cyclic loading at high temperature, *Model. Simul. Mater. Sci. Eng.* 24 (2016). doi:10.1088/0965-0393/24/5/055009.
- [25] V.T. Phan, X. Zhang, Y. Li, C. Oskay, Microscale modeling of creep deformation and rupture in Nickel-based superalloy IN 617 at high temperature, *Mech. Mater.* 114 (2017) 215–227. doi:10.1016/j.mechmat.2017.08.008.
- [26] P. Eisenlohr, M. Diehl, R.A. Lebensohn, F. Roters, A spectral method solution to crystal elasto-viscoplasticity at finite strains, *Int. J. Plast.* 46 (2013) 37–53. doi:10.1016/j.ijplas.2012.09.012.
- [27] R.A. Lebensohn, A.K. Kanjarla, P. Eisenlohr, An elasto-viscoplastic formulation based on fast Fourier transforms for the prediction of micromechanical fields in polycrystalline materials, *Int. J. Plast.* 32–33 (2012) 59–69. doi:10.1016/j.ijplas.2011.12.005.
- [28] D.C. Ahn, P. Sofronis, R. Minich, On the micromechanics of void growth by prismatic-dislocation loop emission, *J. Mech. Phys. Solids.* 54 (2006) 735–755. doi:10.1016/j.jmps.2005.10.011.
- [29] A. Pineau, A.A. Benzerga, T. Pardoen, Failure of metals I: Brittle and ductile fracture, *Acta Mater.* 107 (2016) 424–483. doi:10.1016/j.actamat.2015.12.034.
- [30] M. Knezevic, R.J. McCabe, R.A. Lebensohn, C.N. Tomé, C. Liu, M.L. Lovato, B. Mihaila, Integration of self-consistent polycrystal plasticity with dislocation density based hardening laws within an implicit finite element framework: Application to low-symmetry metals, *J. Mech. Phys. Solids.* 61 (2013) 2034–2046. doi:10.1016/j.jmps.2013.05.005.
- [31] R.J. McCabe, L. Capolungo, P.E. Marshall, C.M. Cady, C.N. Tomé, Deformation of wrought uranium: Experiments and modeling, *Acta Mater.* 58 (2010) 5447–5459. doi:10.1016/j.actamat.2010.06.021.
- [32] K. Kitayama, C.N. Tomé, E.F. Rauch, J.J. Gracio, F. Barlat, A crystallographic dislocation model for describing hardening of polycrystals during strain path changes. Application to low carbon steels, *Int. J. Plast.* 46 (2013) 54–69. doi:10.1016/j.ijplas.2012.09.004.
- [33] M. Zecevic, M. Knezevic, A dislocation density based elasto-plastic self-consistent model for the prediction of cyclic deformation: Application to AA6022-T4, *Int. J. Plast.* 72 (2015) 200–

217. doi:10.1016/j.ijplas.2015.05.018.
- [34] M. Knezevic, J. Crapps, I.J. Beyerlein, D.R. Coughlin, K.D. Clarke, R.J. McCabe, Anisotropic modeling of structural components using embedded crystal plasticity constitutive laws within finite elements, *Int. J. Mech. Sci.* 105 (2016) 227–238. doi:10.1016/j.ijmecsci.2015.11.021.
- [35] M. Knezevic, R.J. McCabe, C.N. Tomé, R.A. Lebensohn, S.R. Chen, C.M. Cady, G.T. Gray, B. Mihaila, Modeling mechanical response and texture evolution of alpha-uranium as a function of strain rate and temperature using polycrystal plasticity, *Int. J. Plast.* 43 (2013) 70–84. doi:10.1016/j.ijplas.2012.10.011.
- [36] C. Reuber, P. Eisenlohr, F. Roters, D. Raabe, Dislocation density distribution around an indent in single-crystalline nickel: Comparing nonlocal crystal plasticity finite-element predictions with experiments, *Acta Mater.* 71 (2014) 333–348. doi:10.1016/j.actamat.2014.03.012.
- [37] J.W. Wilkerson, K.T. Ramesh, A dynamic void growth model governed by dislocation kinetics, *J. Mech. Phys. Solids.* 70 (2014) 262–280. doi:10.1016/j.jmps.2014.05.018.
- [38] G.D. Nguyen, A.M. Korsunsky, J.P.H. Belnoue, A nonlocal coupled damage-plasticity model for the analysis of ductile failure, *Int. J. Plast.* 64 (2015) 56–75. doi:10.1016/j.ijplas.2014.08.001.
- [39] A. Mbiakop, A. Constantinescu, K. Danas, An analytical model for porous single crystals with ellipsoidal voids, *J. Mech. Phys. Solids.* 84 (2015) 436–467. doi:10.1016/j.jmps.2015.07.011.
- [40] M. Basirat, T. Shrestha, G.P. Potirniche, I. Charit, K. Rink, A study of the creep behavior of modified 9Cr-1Mo steel using continuum-damage modeling, *Int. J. Plast.* 37 (2012) 95–107. doi:10.1016/j.ijplas.2012.04.004.
- [41] S. Kruch, J.L. Chaboche, Multi-scale analysis in elasto-viscoplasticity coupled with damage, in: *Int. J. Plast.*, 2011: pp. 2026–2039. doi:10.1016/j.ijplas.2011.03.007.
- [42] L. Malcher, E.N. Mamiya, An improved damage evolution law based on continuum damage mechanics and its dependence on both stress triaxiality and the third invariant, *Int. J. Plast.* 56 (2014) 232–261. doi:10.1016/j.ijplas.2014.01.002.
- [43] A. Shojaei, G.Z. Voyiadjis, P.J. Tan, Viscoplastic constitutive theory for brittle to ductile damage in polycrystalline materials under dynamic loading, *Int. J. Plast.* 48 (2013) 125–151. doi:10.1016/j.ijplas.2013.02.009.
- [44] Y. Alinaghian, M. Asadi, A. Weck, Effect of pre-strain and work hardening rate on void growth and coalescence in AA5052, *Int. J. Plast.* 53 (2014) 193–205. doi:10.1016/j.ijplas.2013.08.007.
- [45] M. Brünig, S. Gerke, V. Hagenbrock, Micro-mechanical studies on the effect of the stress triaxiality and the Lode parameter on ductile damage, *Int. J. Plast.* 50 (2013) 49–65. doi:10.1016/j.ijplas.2013.03.012.
- [46] A. Kami, B.M. Dariani, A. Sadough Vanini, D.S. Comsa, D. Banabic, Numerical determination of the forming limit curves of anisotropic sheet metals using GTN damage model, *J. Mater. Process. Technol.* 216 (2015) 472–483. doi:10.1016/j.jmatprotec.2014.10.017.
- [47] D. Paquet, S. Ghosh, Microstructural effects on ductile fracture in heterogeneous materials. Part I: Sensitivity analysis with LE-VCFEM, *Eng. Fract. Mech.* 78 (2011) 205–225. doi:10.1016/j.engfracmech.2010.07.009.
- [48] A. Hosokawa, H. Toda, R. Batres, H. Li, O. Kuwazuru, M. Kobayashi, H. Yakita, Ductile fracture via hydrogen pore mechanism in an aluminum alloy; quantitative microstructural analysis and image-based finite element analysis, *Mater. Sci. Eng. A.* 671 (2016) 96–106. doi:10.1016/j.msea.2016.06.037.
- [49] T.W.J. de Geus, R.H.J. Peerlings, M.G.D. Geers, Microstructural modeling of ductile fracture

- initiation in multi-phase materials, *Eng. Fract. Mech.* 147 (2015) 318–330. doi:10.1016/j.engfracmech.2015.04.010.
- [50] F. Hannard, T. Pardoen, E. Maire, C. Le Bourlot, R. Mokso, A. Simar, Characterization and micromechanical modelling of microstructural heterogeneity effects on ductile fracture of 6xxx aluminium alloys, *Acta Mater.* 103 (2016) 558–572. doi:10.1016/j.actamat.2015.10.008.
- [51] W. Huang, Q. Huo, Z. Fang, Z. Xiao, Y. Yin, Z. Tan, X. Yang, Damage analysis of hot-rolled AZ31 Mg alloy sheet during uniaxial tensile testing under different loading directions, *Mater. Sci. Eng. A.* 710 (2018) 289–299. doi:10.1016/j.msea.2017.10.108.
- [52] M.H. Shaeri, M. Shaeri, M.T. Salehi, S.H. Seyyedain, F. Djavanrodi, Microstructure and texture evolution of Al-7075 alloy processed by equal channel angular pressing, *Trans. Nonferrous Met. Soc. China.* 25 (2015) 1367–1375. doi:10.1016/S1003-6326(15)63735-9.
- [53] P. Hu, Y. Liu, Y. Zhu, L. Ying, Crystal plasticity extended models based on thermal mechanism and damage functions: Application to multiscale modeling of aluminum alloy tensile behavior, *Int. J. Plast.* 86 (2016) 1–25. doi:10.1016/j.ijplas.2016.07.001.
- [54] F.P.E. Dunne, D. Rugg, A. Walker, Lengthscale-dependent, elastically anisotropic, physically-based hcp crystal plasticity: Application to cold-dwell fatigue in Ti alloys, *Int. J. Plast.* 23 (2007) 1061–1083. doi:10.1016/j.ijplas.2006.10.013.
- [55] T. Zhang, D.M. Collins, F.P.E. Dunne, B.A. Shollock, Crystal plasticity and high-resolution electron backscatter diffraction analysis of full-field polycrystal Ni superalloy strains and rotations under thermal loading, *Acta Mater.* 80 (2014) 25–38. doi:10.1016/j.actamat.2014.07.036.
- [56] M. Ardeljan, I.J. Beyerlein, M. Knezevic, A dislocation density based crystal plasticity finite element model: Application to a two-phase polycrystalline HCP/BCC composites, *J. Mech. Phys. Solids.* 66 (2014) 16–31. doi:10.1016/j.jmps.2014.01.006.
- [57] N. Ono, R. Nowak, S. Miura, Effect of deformation temperature on Hall-Petch relationship registered for polycrystalline magnesium, *Mater. Lett.* 58 (2004) 39–43. doi:10.1016/S0167-577X(03)00410-5.
- [58] E.R.F. Lqyd, A.L. Kleinman, 5p K Iyengar, G. Venkataraman, P.R. Vijayarag-Havan, A.P. Roy, Y.P. Varshni, Temperature Dependence of the Elastic Constants, P. R. Antoniewicz L. Kleinmann *Phys. Rev. Proc. Roy. Soc. Phys. Rev.* ~42<sup>1</sup> J. L. Falicov, *Proc. Roy. Soc. Phys. Rev. B.* 215 (1962) 40–215. doi:10.1103/PhysRevB.2.3952.
- [59] S.R. Chen, G.T. Gray, Constitutive behavior of tantalum and tantalum-tungsten alloys, *Metall. Mater. Trans. A.* 27 (1996) 2994–3006. doi:10.1007/BF02663849.
- [60] D.M. Goto, R.K. Garrett, J.F. Bingert, S.R. Chen, G.T. Gray, The mechanical threshold stress constitutive-strength model description of HY-100 steel, *Metall. Mater. Trans. A.* 31 (2000) 1985–1996. doi:10.1007/s11661-000-0226-8.
- [61] B. Svendsen, S. Bargmann, On the continuum thermodynamic rate variational formulation of models for extended crystal plasticity at large deformation, *J. Mech. Phys. Solids.* 58 (2010) 1253–1271. doi:10.1016/j.jmps.2010.06.005.
- [62] S. Ghosh, A. Shahba, X. Tu, E.L. Huskins, B.E. Schuster, Crystal plasticity FE modeling of Ti alloys for a range of strain-rates. Part II: Image-based model with experimental validation, *Int. J. Plast.* 87 (2016) 48–68. doi:10.1016/j.ijplas.2016.09.003.
- [63] P. Lin, Z. Liu, Z. Zhuang, Numerical study of the size-dependent deformation morphology in micropillar compressions by a dislocation-based crystal plasticity mode, *Int. J. Plast.* 87 (2016)

- 32–47. doi:10.1016/j.ijplas.2016.09.001.
- [64] A. Khosravani, J. Scott, M.P. Miles, D. Fullwood, B.L. Adams, R.K. Mishra, Twinning in magnesium alloy AZ31B under different strain paths at moderately elevated temperatures, *Int. J. Plast.* 45 (2013) 160–173. doi:10.1016/j.ijplas.2013.01.009.
- [65] I.J. Beyerlein, C.N. Tomé A dislocation-based constitutive law for pure Zr including temperature effects, *Int. J. Plast.* 24 (2008) 867–895. doi:10.1016/j.ijplas.2007.07.017.
- [66] L. Capolungo, I.J. Beyerlein, G.C. Kaschner, C.N. Tomé On the interaction between slip dislocations and twins in HCP Zr, *Mater. Sci. Eng. A.* 513–514 (2009) 42–51. doi:10.1016/j.msea.2009.01.035.
- [67] D. Kuhlmann-Wilsdorf, The theory of dislocation-based crystal plasticity, *Philos. Mag. A Phys. Condens. Matter, Struct. Defects Mech. Prop.* 79 (1999) 955–1008. doi:10.1080/01418619908210342.
- [68] C. Jean, Lemaitre; Jean-Louis, ASPECT PHENOMENOLOGIQUE DE LA RUPTURE PAR ENDOMMAGEMENT, *J. Mécanique Appliquée.* 2 (1978) 317–65. <http://worldcat.org/issn/03990842>.
- [69] M. Mengoni, J.P. Ponthot, A generic anisotropic continuum damage model integration scheme adaptable to both ductile damage and biological damage-like situations, *Int. J. Plast.* 66 (2015) 46–70. doi:10.1016/j.ijplas.2014.04.005.
- [70] X. min ZHANG, W. dong ZENG, Y. SHU, Y. gang ZHOU, Y. qing ZHAO, H. WU, H. qing YU, Fracture criterion for predicting surface cracking of Ti40 alloy in hot forming processes, *Trans. Nonferrous Met. Soc. China (English Ed.)* 19 (2009) 267–271. doi:10.1016/S1003-6326(08)60263-0.
- [71] P. Rosakis, A.J. Rosakis, G. Ravichandran, J. Hodowany, Thermodynamic internal variable model for the partition of plastic work into heat and stored energy in metals, *J. Mech. Phys. Solids.* 48 (2000) 581–607. doi:10.1016/S0022-5096(99)00048-4.
- [72] L. Anand, M.E. Gurtin, Thermal effects in the superelasticity of crystalline shape-memory materials, *J. Mech. Phys. Solids.* 51 (2003) 1015–1058. doi:10.1016/S0022-5096(03)00017-6.
- [73] Y. Huang, A user-material subroutine incorporating single crystal plasticity in the ABAQUS finite element program.pdf, (1991). [http://www.columbia.edu/~jk2079/Kysar\\_Research\\_Laboratory/Single\\_Crystal\\_UMAT.html](http://www.columbia.edu/~jk2079/Kysar_Research_Laboratory/Single_Crystal_UMAT.html).
- [74] E.B. Marin, P.R. Dawson, Elastoplastic finite element analyses of metal deformations using polycrystal constitutive models, *Comput. Methods Appl. Mech. Eng.* 165 (1998) 23–41. doi:10.1016/S0045-7825(98)00033-4.
- [75] R. Quey, P.R. Dawson, F. Barbe, Large-scale 3D random polycrystals for the finite element method: Generation, meshing and remeshing, *Comput. Methods Appl. Mech. Eng.* 200 (2011) 1729–1745. doi:10.1016/j.cma.2011.01.002.
- [76] I. Simonovski, L. Cizelj, N. Jakšić, The influence of finite element meshes on the results of a spatial polycrystalline aggregate model, *Nucl. Eng. Des.* 241 (2011) 1184–1190. doi:10.1016/j.nucengdes.2010.05.063.
- [77] J.R. Mayeur, I.J. Beyerlein, C.A. Bronkhorst, H.M. Mourad, Incorporating interface affected zones into crystal plasticity, *Int. J. Plast.* 65 (2015) 206–225. doi:10.1016/j.ijplas.2014.08.013.
- [78] I. Benedetti, M.H. Aliabadi, A three-dimensional cohesive-frictional grain-boundary micromechanical model for intergranular degradation and failure in polycrystalline materials, *Comput. Methods Appl. Mech. Eng.* 265 (2013) 36–62. doi:10.1016/j.cma.2013.05.023.

- [79] J. Rossiter, A. Brahme, K. Inal, R. Mishra, Numerical analyses of surface roughness during bending of FCC single crystals and polycrystals, *Int. J. Plast.* 46 (2013) 82–93. doi:10.1016/j.ijplas.2013.01.016.
- [80] A. Masud, T.J. Truster, A framework for residual-based stabilization of incompressible finite elasticity: Stabilized formulations and F methods for linear triangles and tetrahedra, *Comput. Methods Appl. Mech. Eng.* 267 (2013) 359–399. doi:10.1016/j.cma.2013.08.010.
- [81] J. Cheng, A. Shahba, S. Ghosh, Stabilized tetrahedral elements for crystal plasticity finite element analysis overcoming volumetric locking, *Comput. Mech.* 57 (2016) 733–753. doi:10.1007/s00466-016-1258-2.
- [82] R.W. Armstrong, 60 Years of Hall-Petch: Past to Present Nano-Scale Connections, *Mater. Trans.* 55 (2014) 2–12. doi:10.2320/matertrans.MA201302.
- [83] V. Picheny, Multiobjective optimization using Gaussian process emulators via stepwise uncertainty reduction, *Stat. Comput.* 25 (2015) 1265–1280. doi:10.1007/s11222-014-9477-x.
- [84] M. Seeger, Gaussian processes for machine learning, *Int. J. Neural Syst.* 14 (2004) 69–106. doi:10.1142/S0129065704001899.
- [85] Y. Bao, T. Wierzbicki, On fracture locus in the equivalent strain and stress triaxiality space, *Int. J. Mech. Sci.* 46 (2004) 81–98. doi:10.1016/j.ijmecsci.2004.02.006.
- [86] J.B. Kim, J.W. Yoon, Analysis of the Necking Behaviors with the Crystal Plasticity Model Using 3-Dimensional Shaped Grains, *Adv. Mater. Res.* 684 (2013) 357–361. doi:10.4028/www.scientific.net/AMR.684.357.
- [87] M. Kashfuddoja, M. Ramji, Assessment of local strain field in adhesive layer of an unsymmetrically repaired CFRP panel using digital image correlation, *Int. J. Adhes. Adhes.* 57 (2015) 57–69. doi:10.1016/j.ijadhadh.2014.10.005.
- [88] T.F. Morgeneyer, T. Taillandier-Thomas, A. Buljac, L. Helfen, F. Hild, On strain and damage interactions during tearing: 3D in situ measurements and simulations for a ductile alloy (AA2139-T3), *J. Mech. Phys. Solids.* 96 (2016) 550–571. doi:10.1016/j.jmps.2016.07.012.
- [89] C. Oskay, M. Haney, Computational modeling of titanium structures subjected to thermo-chemo-mechanical environment, *Int. J. Solids Struct.* 47 (2010) 3341–3351. doi:10.1016/j.ijsolstr.2010.08.014.
- [90] C. Nihare, P.D. Hodgson, M. Weiss, Necking and fracture of advanced high strength steels, *Mater. Sci. Eng. A.* 528 (2011) 3010–3013. doi:10.1016/j.msea.2010.12.098.
- [91] N. Bonora, D. Gentile, A. Pirondi, G. Newaz, Ductile damage evolution under triaxial state of stress: Theory and experiments, *Int. J. Plast.* 21 (2005) 981–1007. doi:10.1016/j.ijplas.2004.06.003.
- [92] H. Proudhon, J. Li, F. Wang, A. Roos, V. Chiaruttini, S. Forest, 3D simulation of short fatigue crack propagation by finite element crystal plasticity and remeshing, in: *Int. J. Fatigue*, 2016: pp. 238–246. doi:10.1016/j.ijfatigue.2015.05.022.
- [93] S.J. Marcadet, D. Mohr, Effect of compression-tension loading reversal on the strain to fracture of dual phase steel sheets, *Int. J. Plast.* 72 (2015) 21–43. doi:10.1016/j.ijplas.2015.05.002.
- [94] Z. Zheng, D.S. Balint, F.P.E. Dunne, Discrete dislocation and crystal plasticity analyses of load shedding in polycrystalline titanium alloys, *Int. J. Plast.* 87 (2016) 15–31. doi:10.1016/j.ijplas.2016.08.009.
- [95] M. Diehl, M. Wicke, P. Shanthraj, F. Roters, A. Brueckner-Foit, D. Raabe, Coupled Crystal Plasticity–Phase Field Fracture Simulation Study on Damage Evolution Around a Void: Pore

- Shape Versus Crystallographic Orientation, *JOM*. 69 (2017) 872–878. doi:10.1007/s11837-017-2308-8.
- [96] A. Patra, D.L. McDowell, A void nucleation and growth based damage framework to model failure initiation ahead of a sharp notch in irradiated bcc materials, *J. Mech. Phys. Solids*. 74 (2015) 111–135. doi:10.1016/j.jmps.2014.10.006.
- [97] C. Teko lu, J.W. Hutchinson, T. Pardoen, On localization and void coalescence as a precursor to ductile fracture, *Philos. Trans. R. Soc. A Math. Phys. Eng. Sci.* 373 (2015) 20140121–20140121. doi:10.1098/rsta.2014.0121.
- [98] S. Zhang, C. Oskay, Reduced order variational multiscale enrichment method for thermo-mechanical problems, *Comput. Mech.* 59 (2017) 887–907. doi:10.1007/s00466-017-1380-9.
- [99] X. Zhang, C. Oskay, Eigenstrain based reduced order homogenization for polycrystalline materials, *Comput. Methods Appl. Mech. Eng.* 297 (2015) 408–436. doi:10.1016/j.cma.2015.09.006.